

https://dspace.org/

Fullerenes, carbon nanotubes and graphene as tetrel bond donors and acceptors of electrophiles

Varadwaj, Pradeep R.; Varadwaj, Arpita; Marques, Helder; Yamashita, Koichi

2023-05
Royal Society of Chemistry
https://hdl.handle.net/10539/50255
Pradeep R. Varadwaj, Arpita Varadwaj, Helder Marques, Koichi Yamashita; Fullerenes, carbon nanotubes and graphene as tetrel bond donors and acceptors of electrophiles. CrystEngComm 2023; 25 (23): 3417–3438. https://doi.org/10.1039/d3ce00184a

Downloaded from a DSpace repository. https://dspace.org/

CrystEngComm

ROYAL SOCIETY OF CHEMISTRY

PAPER

Published on 10 May 2023
Licence and permissions

Check for updates

Cite this: *CrystEngComm*, 2023, **25**, 3417

Fullerenes, carbon nanotubes and graphene as tetrel bond donors and acceptors of electrophiles†

Pradeep R. Varadwaj, *[ab] Arpita Varadwaj, [a] Helder Marques [b] and Koichi Yamashita [a]

The signs of the extrema of the molecular electrostatic surface potential (MESP) are an effective means of probing the surface reactivity behavior of molecules. They determine the electrophilicity and nucleophilicity regions, which collectively explain why one polar region of the surface of a given molecule attracts another region of opposite polarity in the same or in a neighboring molecule, resulting in the formation of molecular complexes or supramolecular assemblies in large-scale chemical systems. The chemical systems discussed in this paper are derivatives of fullerenes, carbon nanotubes and a few allotropes of graphene, that have been extensively explored, both theoretically and experimentally, to form a variety of functional materials for application in various fields of chemistry, biology, and polymer and nanomaterials science. We show, using the MESP model, that these highly-valued delocalized systems feature electron-rich and electron-deficient π-regions that can be regarded as negative and positive π-holes, respectively. The former and latter may be regarded as efficient π-hole acceptors of electrophiles (*viz.* a hydrogen bond) and tetrel bond donors, respectively, when in close proximity with the same or different chemical systems in the crystalline phase. The appearance of negative regions on the surface of the C═C bonding region of the chemical systems considered for investigation was found to be consistent with the relatively large delocalization index of the corresponding bond, revealed using the quantum theory of atoms in molecules. Some dimers of C_{20}, C_{60} and C_{70} fullerene systems with commonly known diatomic molecules (N_2, CO, HX and X_2 (X = F, Cl, Br) and F_2, *etc.*) are investigated to illustrate the concept developed above.

Received 24th February 2023,
Accepted 9th May 2023

DOI: 10.1039/d3ce00184a

rsc.li/crystengcomm

Introduction

Carbonaceous materials have received considerable attention since the latter half of the last century,[1] leading to a myriad of discoveries applicable for a carbon-neutral society.[2–5] Applications range from crystallography to nanotechnologies and devices in the area of sustainable energy[6] and sensors for biomaterials preparation (as energy conversion and storage electrodes, or as effluent remediation sorbents (for electrocatalysis[7])).

Buckminsterfullerene C_{60} and its derivatives (often colloquially referred to as buckyballs), and carbon nanotubes (CNTs), are a specific class of carbonaceous materials. They consist of closed fragments of graphite.[8] These, together with graphene and its allotropes, are a popular class of nanofiller for biological[9] and carbon-fiber reinforced polymeric nanocomposite materials,[10–13] central to the development of many carbonaceous nanomaterials. For instance, C_{60} and its reinforced derivatives are used for polymer- and organic solar cells[14,15] and for semiconductor devices.[16–18] Their application as photocatalyst enhancers is also known,[19] used in many biomedical applications.[20–23] Similarly, CNTs are highly conductive systems, with strong C═C bonds, with complex, unique mechanisms of charge carrier movement, and large surface energy.[24] Single-walled CNTs are the focus of much current research because of their structure (chirality) and exceptional physical properties such as metallic-to-semiconducting phase transitions,[25,26] resulting in a wide range of applications.[12,26–32] The semi-metallic, honeycomb-like Dirac material graphene,[33,34] and its allotropes are also conductive and have attracted attention in, for example, energy storage devices such as supercapacitors and lithium-ion batteries,[35–37] in energy generation systems,[38,39] and sensors.[40,41]

This study was prompted by the belief that there are specific sites on these carbonaceous systems that are locales for nucleophilic and electrophilic attack and are important

[a] *Department of Chemical System Engineering, School of Engineering, The University of Tokyo 7-3-1, Tokyo 113-8656, Japan. E-mail: pradeep@t.okayama-u.ac.jp*
[b] *Molecular Sciences Institute, School of Chemistry, University of the Witwatersrand, Johannesburg 2050, South Africa*

† Electronic supplementary information (ESI) available. See DOI: https://doi.org/10.1039/d3ce00184a

for the development of ordered, self-assembling functional materials. For instance, using vacuum thermal evaporation, Burlingame *et al.*[42] demonstrated a photoactive organic heterostructure comprising a thin fullerene channel sandwiched between an electron-blocking layer and a blended donor C_{70} fullerene heterojunction that generates charges by dissociating excitons. To this end, it would be interesting to understand what causes identical buckyballs to stay in close proximity to each other leading to the formation of a layered thin film of fullerenes. Besides, and as illustrated below, there are hundreds of carbonaceous systems catalogued in the Cambridge Structural Database (CSD)[43,44] in which fullerenes and their derivatives, together with other molecules, act as building blocks that play a vital role in shaping these bulk systems in the crystalline phase.

In this study we have attempted to shed light on the molecular surface reactivity of a series of fullerenes (from C_{20} to C_{70}), CNTs of various chirality, and some allotropes of graphene. In particular, we discuss the potential ability of these systems as tetrel bond donors and acceptors of electrophiles.

A tetrel bond occurs when there is evidence of a net attractive interaction between an electrophilic region associated with a covalently or coordinately bonded tetrel atom in a molecule and a nucleophilic region in another, or the same, molecule. A list of its featured properties and occurrence of its chemical instances in crystalline systems have recently been discussed.[45]

Tetrel bonds formed by molecules may be σ-hole or π-hole centered. They can be formed when the "hole" on the bonded tetrel atom (or atoms) is electrophilic, described by a positive electrostatic surface potential, and coulombically engaged with a negative site on the same or on a neighboring molecule. A σ-hole on a tetrel atom may be observed on its surface (for example, C in CF_3Cl and CBr_4) along the outermost extension of the covalent bond involving the atom; it can be positive or negative. However, π-holes, which can also be positive or negative, are often observed in delocalized systems, which can be readily seen on the (centroid surface of) six-membered carbon framework, a halogenated benzene derivative, or a fullerene C_{60} molecule. Other occasions where an electrophilic π-hole on the surface of a molecule can be observed are outlined in the following section.

We utilized two contemporary theoretical tools to explore the reactive surface chemistry of the carbonaceous systems: the molecular electrostatic surface potential (MESP)[46–51] and quantum theory of atoms in molecules (QTAIM) approaches.[52–54] The details of these two approaches have been discussed in many research papers (for example ref. 55–59), reviews (for example ref. 46–51) and overviews.[56,60–63] We have also carried out second-order natural bond orbital (NBO) analysis[64] and independent gradient model (IGM-δg^{inter})[65,66] based charge-density isosurface analysis on specific binary complex systems to demonstrate the occurrence of intermolecular interactions in them. QTAIM-based delocalization indices were utilized to demonstrate their link with the extrema of MESP. The details of these computational methodologies are discussed in the ESI.†

Results

Electrostatic surfaces of fullerene derivatives as tetrel bond donors

The C_{20} molecule. The fullerene, C_{20}, with I_h point-group symmetry, is the smallest experimentally characterized and most structurally-strained member of the fullerene family.[67] It consists of 12 pentagonal C_5 rings that form a dodecahedral carbon cage structure with no hexagonal rings incorporated, resulting in a species with extreme curvature.[68] Solid C_{20} fullerene is a promising candidate for use as a high-temperature superconductor due to its larger electron–phonon coupling, higher than that of C_{60} itself.[69] It is one of the most active classes of nanostructures, and has been widely used as a material for important applications.[70]

QTAIM's delocalization index δ is not the same for each of the five C–C atom-atom pairs in the C_5 rings in C_{20}. In each ring, three comprise alternate C═C double bonds (δ values between 1.2–1.4), and the remainder two comprise C–C single bonds (δ values between 0.97–1.10). The results of the MESP calculation, Fig. 1a, suggest that the surface of the centroid regions of each of the 12 pentagonal C_5 rings is electrophilic, which is characteristic of a tetrel-centered electrophilic π-hole. Their $V_{S,max}$ values are different (8.0/9.0 and 11.2 kcal mol^{-1}) because of a non-uniform distribution of charge density on the electrostatic surface of the molecule. The local most potential minima appearing around surfaces of the C–C bond regions are not all nucleophilic; $V_{S,min}$ associated with some them are positive (values between 5.7 and 6.1 kcal mol^{-1}), and others

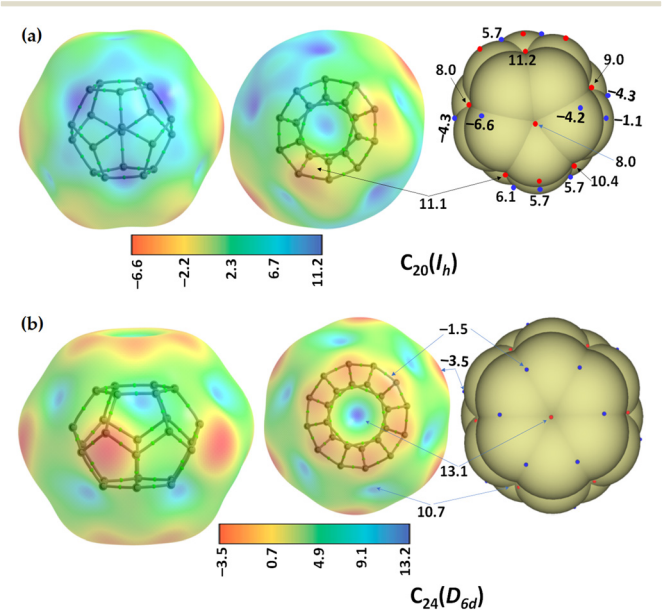


Fig. 1 The electrostatic surface potential plots of a) C_{20} and b) C_{24} molecules mapped with their corresponding 0.001 a.u. isoelectron density envelopes, obtained with ωB97X-D/cc-pVTZ. Two different views are shown for each case (left), with the values in the color bar in kcal mol^{-1}. An approximate van der Waals surface is shown for each case (right), with the local most minima and maxima ($V_{S,min}$ and $V_{S,max}$), depicted as tiny circles in blue and red, respectively.

This journal is © The Royal Society of Chemistry 2023

(especially those having C=C delocalized bonds with δ values 1.35 and 1.41) are negative ($V_{S,min}$ values between −1.1 and −6.6 kcal mol^{-1}). These results indicate that C_{20} is a potential tetrel bond donor, rather than a potential tetrel bond acceptor (or an acceptor of electrophiles). Although this is the result obtained with the cc-PVTZ basis set, our conclusions about the tetrel bond donating capacity of C_{20} remain unchanged even when basis sets of different quality are used to calculate the extrema of the potential and their characters. The data in Table 1 show that the sign of the extrema of potential does not change, but the quality of the basis set employed has a marginal effect on the magnitude of the potential. The data indicate that there are two types of π-holes on the outer electrostatic surface of C_{20} with different values of the local most maximum of potential around the centroid region of the C_5 rings; the negative potential is mostly concentrated on the surface of the C=C bonding region or on C's surface. This result is consistent with the finding of the study of Politzer and co-workers,[71] in which the choice of basis set does not affect the (positive or negative) character of the potential extrema of the chemical system, but only their magnitudes. The tetrel bond donor or acceptor nature of any carbonaceous system is determined solely by the sign of the extrema of potential, while the magnitude of the potential determines the strength.

The C_{24} molecule. C_{24}, with D_{6d} symmetry, is the next smallest fullerene system[72,73] and has been characterized experimentally and detected in space;[74] its structure in other space groups (D_6 and O_h) is theoretically known.[75] It consists of 12 C_5 rings and two C_6 rings. The non-covalent reactivity of its outer surface with guest species, such as the drug ephedrine, has been investigated theoretically,[76] and it was suggested that it is a potential carrier for this drug. A QTAIM analysis suggests that the C_6 rings contain delocalized C=C bonds, evidenced by δ values of 1.31–1.40 between each pair of bonded C atoms. This was not so for the 12 C_5 rings. Our calculation suggested that two out of five C–C pairs in each C_5 ring have double bond character (δ values between 1.30 and 1.54), and the remaining three have single-bond character (δ values between 0.997 and 1.055).

The MESP analysis, Fig. 1b, shows that the centroid region of each C_5 and C_6 rings is electrophilic, the latter more so than the former ($V_{S,max}$ values 10.7 kcal mol^{-1} *vs.* 13.1 kcal mol^{-1}). These are the electrophilic π-holes that emerge from the p-orbitals of the bonded carbon atoms orthogonal to the C–C and C=C bonds in C_{24}. The outer surfaces of the C=C delocalized bonds of each of the two C_6 rings have δ values in the range 1.305–1.400 and are weakly nucleophilic, with $V_{S,min}$ = −1.5 kcal mol^{-1}. The central portion of the C=C delocalized bond between two nearest C_5 sites is nucleophilic ($V_{S,min}$ = −3.5 kcal mol^{-1}). These results indicate that C_{24} is probably a better π-hole centered tetrel bond donor than C_{20}, even though the surface of C_{24} is segmented into various positive and negative regions compared to the surface of C_{20}.

Although fullerene derivatives, such as C_n ($26 \leq n \leq 60$; $n \in 2Z$), have been theoretically predicted, and some have been experimentally produced, we limited our study to C_{44}, C_{50}, C_{60} and C_{70}; the last two are very well known and have found application in diverse areas of chemistry, physics, biology, polymer and materials science.

The C_{44} molecule. There are 89 isomers of C_{44} that have been theoretically predicted to possess a variety of point groups.[77–79] The QTAIM-based molecular graph of the C_{44} isomer with C_2 symmetry is shown in Fig. 2a (top). It consists of 12 pentagons and 12 hexagons. The delocalization index for the carbon–carbon pairs of the C_5 and C_6 rings of C_{44} ranges from 1.0 to 1.52. Assessing the aromatic nature of these rings is not straightforward without performing robust analysis involving HOMA (harmonic oscillator model of aromaticity)[80–82] and other indices,[83,84] which is beyond the course of this study. Nevertheless, the MESP model calculations suggest that the sign of the potential of the centroid regions of all the carbon rings are positive ($V_{S,max} > 0$) regardless of their type (Fig. 2a (top and bottom)); hence each of them could serve as a π-hole centered tetrel bond donor. The electrostatic surfaces of C–C bonds with delocalization indices >1.2, which are seen in the end-capped C_5 rings, are found to be associated with negative potential ($V_{S,min} < 0$); they could act as tetrel bond acceptors, as well as an acceptor of an electrophile (*e.g.*, a halogen bond, a hydrogen bond, or a chalcogen bond, *etc.*).

The C_{50} molecule. Hundreds of isomers of C_{50} are theoretically possible.[85–87] We have considered one, the

Table 1 Basis set dependence of selected (0.001 a.u. isoelectronic density envelope mapped) extrema of potential (kcal mol^{-1}) on the surface of C_{20} fullerene, obtained using ωB97X-D in conjunction with nine (Dunning's and Gaussian-type) basis sets of double- and triple-ζ qualities[a]

	Dunning's basis set				Gaussian basis sets				
	cc-pVDZ	aug-cc-pVDZ	cc-pVTZ	aug-cc-pVTZ	6-31G(d,p)	6-31++G(d,p)	6-311G(d,p)	6-311++G(d,p)	6-311++G(2d,2p)
	$V_{S,max}$								
Centroid C_5 ring	11.1	10.6	11.2	12.0	11.1	13.5	11.2	12.7	11.6
Centroid C_5 ring	7.5	7.4	9.0	8.8	8.6	11.0	8.1	10.4	9.3
	$V_{S,min}$								
C–C	5.1	6.1	5.7	6.3	4.4	4.5	6.0	4.8	5.8
C=C	−6.6	−6.3	−6.6	−6.3	−6.8	−6.8	−6.5	−6.4	−6.4
C=C	−4.5	−3.9	−4.3	−4.0	−4.7	−4.7	−4.1	−4.3	−4.1

[a] See Fig. 1a (right) for corresponding values obtained with cc-pVTZ.

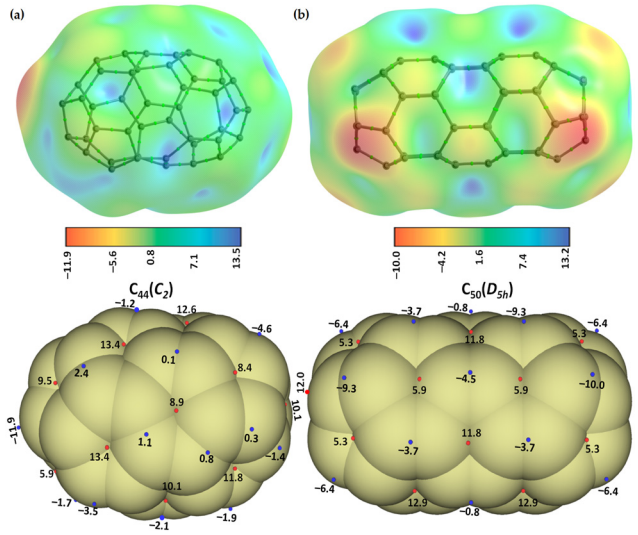


Fig. 2 ωB97X-D/cc-pVTZ calculated electrostatic surface potential plot of a) C_{44} and b) C_{50} fullerene molecules mapped with their corresponding 0.001 a.u. isoelectron density envelopes, with the values in the color bar in kcal mol^{-1}. An approximate van der Waals surface is shown for each case (bottom), with the local most minima and maxima ($V_{S,min}$ and $V_{S,max}$), depicted as tiny circles in blue and red, respectively.

highly symmetric D_{5h} structure. Fig. 2b (top), shows the molecular graph of the tubular form of C_{50} fullerene, superimposed with MESP. It consists of 12 C_5 pentagons and 15 C_6 hexagons. Each end-cap region is surrounded with six pentagons and the central region is built up by 15 hexagons. The aromatic nature of none of these carbon rings is revealed in this work, even though the delocalization index of each of three or four bonds between C atoms in each of the C_6 rings is in the range 1.02–1.15, while the remaining two C pairs in the same ring have a higher delocalization index (δ between 1.29–1.56). Thus, there are both single and double bonds between C atoms in these C_6 rings. The central region of the tubular C_{50} fullerene is more electrophilic than the end-capped portions. Our MESP calculation suggests that the electrophilicity of the centroid region of 12 C_5 rings is variable ($V_{S,max}$ values 5.3, 10.6, 12.0 and 13.2 kcal mol^{-1}), as observed for the C_6 rings ($V_{S,max}$ values 5.9, 11.8, or 12.9 kcal mol^{-1}). Similarly as found for C_{24}, we observed that the surfaces of the C=C bonds with δ between 1.29–1.56 have negative $V_{S,min}$ < 0 ($V_{S,min}$ between −0.8 and −10.9 kcal mol^{-1}), as seen in Fig. 2b (bottom). Other minima of potential found on the surfaces of the CC bonds with low values of δ were positive, with $V_{S,min}$ between 1.3 and 3.5 kcal mol^{-1}.

The C_{60} molecule and its implication in crystals. Isocahedral (I_h) C_{60} is a spherical molecule. It consists of 60 carbon atoms that are sp^2-bonded with each other via delocalized double bonds, forming 12 pentagons and 20 hexagons. The delocalization indices for carbon–carbon pairs are in the range 1.129–1.375, diagnostic of the semi-double character of the C=C bonds. The C=C bonds forming the C_5 rings (δ = 1.129–1.130) are relatively less delocalized than those not involved in the C_5 rings (δ = 1.374). Hence, three C=C bonds in each C_6 ring are inequivalent to the other three because the latter are shared with the three nearest C_5 rings of the C_{60} cage.

The MESP graph of C_{60} (Fig. 3) shows that the center of each C_6 ring (exohedral) surface is electrophilic, as is the C_5 ring. The $V_{S,max}$ of each C_6 ring (all equivalent) is 9.5 kcal mol^{-1}. Similarly, the $V_{S,max}$ of each C_5 ring is 9.6 kcal mol^{-1}; they are not only all equivalent but have virtually identical electrophilicity to the C_6 rings. However, the centroid portion of the 12 C_5 rings in the C_{60} cage interior exhibit strong electrophilicity ($V_{S,max}$ = 23.0 kcal mol^{-1}), indicating that they are a prominent tetrel bond donor. By contrast, the $V_{S,min}$ at the mid portion of an alternate C=C bond in the C_6 ring (outer) is negative ($V_{S,min}$ = −0.93 kcal mol^{-1}). Similarly, there are 30 local potential minima in the interior C_5 and C_6 ring surfaces of the C_{60} cage that are strongly electrophilic, with $V_{S,min}$ = 22.1 kcal mol^{-1}. These results suggest that the C_{60} interior is highly electrophilic, and the centroid portions of the interior surfaces of the C_5 and C_6 rings can be regarded as strong tetrel bond donors.

This result is in disagreement with the views of others who suggested that the electrostatic surface of C_{60} is overall positive,[88,89] and hence compatible with anion–π interactions. The compatibility between them actually emerges from the fact that the positive π-holes on the centroid surface regions of the C_5 and C_6 rings of the C_{60} molecule sustain a coulombic attraction with the anions. It is worth noting that when the carbon atoms are replaced by elements such as N and B, for example, the character of the MESP surface changes in such a way that the surfaces of N and B progressively become more electrophilic. This specific feature has been discussed by Esrafili and coworkers[90] for $C_{59}B$, $C_{58}BN$, $C_{57}BN_2$ and $C_{56}BN_3$, in which the uniformity of charge density distribution observed on the electrostatic surface of the C_{60} is distorted by the substitutions. The N-doped C_{60} fullerene was shown to be a potential cathode catalyst for hydrogen fuel cells.[91] O_2 can be adsorbed and partially reduced on the N–C bonding sites (Pauling sites) of N–C_{60} without any activation barrier. Why this is so may be explained by a MESP model of the system. For instance, adsorption of O_2 takes place at the surface of the C site of the C–N bond in N–C_{60}, a site which is more electrophilic than that of N, *via* coulombic interaction between the lone-pair on O in O=O and electrophilic C. A similar study has also been reported elsewhere.[92]

The MESP description of the surface of C_{60} rationalizes the molecular level packing in the crystal structure of C_{60} (Z = 4),[93,94] Fig. 4a. This is illustrated in Fig. 4b, between three nearest neighbor C_{60} molecules, and was extracted from the unit-cell of the crystal shown in Fig. 4a.

The coulombic attraction between a pair of close-lying C_{60} molecules arises predominantly from $C_5(\pi)\cdots\pi(C{=}C)$ tetrel bonded contacts. This is evident from the atom–atom overlap in the bonding region where the $(C_5)_{centroid}\cdots(C{=}C)_{mid\text{-}point}$ distance is 3.276 Å (Fig. 4b) and is less than twice the van der Waals radius of C, 3.54 Å (r_{vdW}(C) = 1.77 Å (ref. 95)). Although

 This journal is © The Royal Society of Chemistry 2023

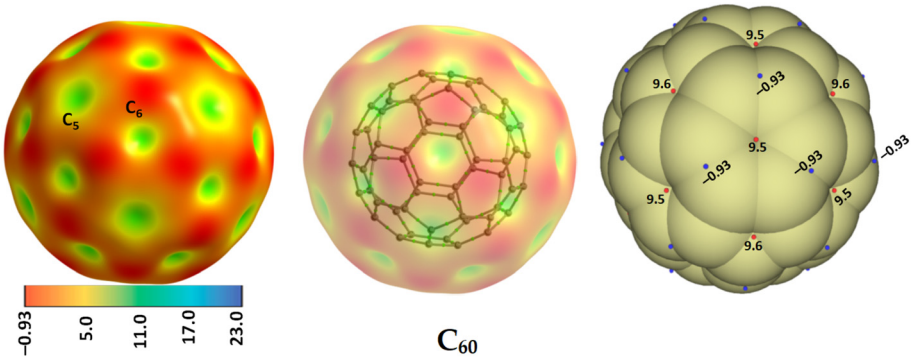


Fig. 3 The electrostatic surface potential plot of the C_{60} molecule 0.001 a.u. mapped with the isoelectronic density envelope, obtained with ωB97X-D/cc-pVTZ. Two different views are shown for each case (left), with the values in the color bar in kcal mol^{-1}. An approximate van der Waals surface is shown for case (right), with the local most minima and maxima ($V_{S,min}$ and $V_{S,max}$), are depicted as tiny circles in blue and red, respectively.

this is the dominant interaction between sites of opposite charge polarity, distorted slipped parallel $C_5(\pi)\cdots\pi(C_6)$ interactions between the $C_5(\pi)$ and $C_6(\pi)$ rings of the interacting C_{60} molecules in the crystal (not shown) are also significant as they occur between interacting sites of unequal charge density.

Examples of crystalline materials in which C_{60} functions as either a tetrel bond donor or a tetrel bond acceptor can be readily seen from Fig. 5. The $C_5(\pi)\cdots\pi(C{=}C)$ interaction between a pair of two C_{60} molecules in the crystal of C_{60} fullerene tetrakis(dimethylamino)ethylene,[96] Fig. 5a, (CSD ref. KUGGIC03 and KUGGIC04), is driven by the attractive interaction between the positive $C_5(\pi)$ of one C_{60} and the negative region localized on the surface of the C=C bond of a neighboring C_{60} molecule. Both the capped stick and capped-stick-and-space-filling models (top and bottom of Fig. 5a, respectively) illustrate the possibility of attraction between interacting moieties. In addition, there are also $H\cdots\pi(C{=}C)$ hydrogen bonded interactions between methyl H sites in $[C(NMe_2)_2]_2$ and $\pi(C{=}C)$ negative π-holes on the C_5 and C_6 frameworks of C_{60} that are responsible for packing of molecules in the crystal (not shown).

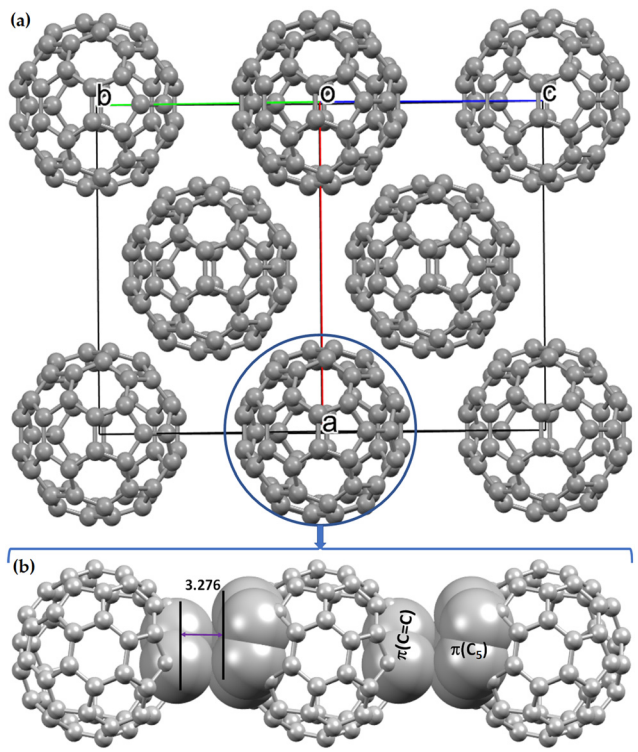


Fig. 4 (a) The unit-cell of the crystal structure of C_{60};[93,94] (b) Representation of a cut from the unit-cell of the same crystal, showing atom-atom overlapping between the close-lying interacting C_{60} molecules. The π-centered tetrel bond distance between the centroid the C_5 ring and the mid-point of the C=C bond is in Å.

In the crystal of bis(4,4′-bromophenyl)-61,61-diylmethano C_{60} fullerene,[97] Fig. 5b, the attraction between the interacting molecules is driven jointly by $C_6(\pi)\cdots$Br tetrel bonding and C–Br$\cdots\pi(C{=}C)$ halogen bonding interactions. The first is due to attraction between the positive $C_6(\pi)$ center and the negative lateral portion of covalently bonded Br; the second arises from the interaction between the positive σ-hole on Br along the outer extension of the C–Br bond in one molecule and the negative π-density on the surface of the C=C bond in the interacting molecule.

In the case of the crystal of C_{60}-fullerene tetramethyltetraselenafulvalene carbon disulfide solvate,[98] Fig. 5c, there are close contacts between solvate CS_2 and the fullerene C_{60} molecule with $C_6(\pi)\cdots$S and $C(\pi)\cdots\pi(C{=}C)$ tetrel bonds. The presence of this interaction is not surprising since the outer surface of S in CS_2 is nucleophilic, which has the ability to act as an electron density donor to interact favorably with the positive $C_6(\pi)$ center of C_{60}, resulting in the formation of a $C_6(\pi)\cdots$S tetrel bond. Similarly, the outer electrostatic surface of C in CS_2 molecule is electrophilic (equipped with a positive π-belt), and this attracts the negative site localized on the surface around the mid-point of the $\pi(C{=}C)$ bond of the C_{60} cage, forming a $C(\pi)\cdots\pi(C{=}C)$ tetrel bond.

As above, the crystal of $C_{60}{\cdot}C_9Cl_9N$ comprises perchloroazatriquinacene, C_9Cl_9N, and C_{60} molecules. They form a host–guest complex.[99] The chalice-like azatriquinacene packs between completely ordered fullerene molecules in the crystal with multiple $C_{60}\cdots$Cl close contacts.

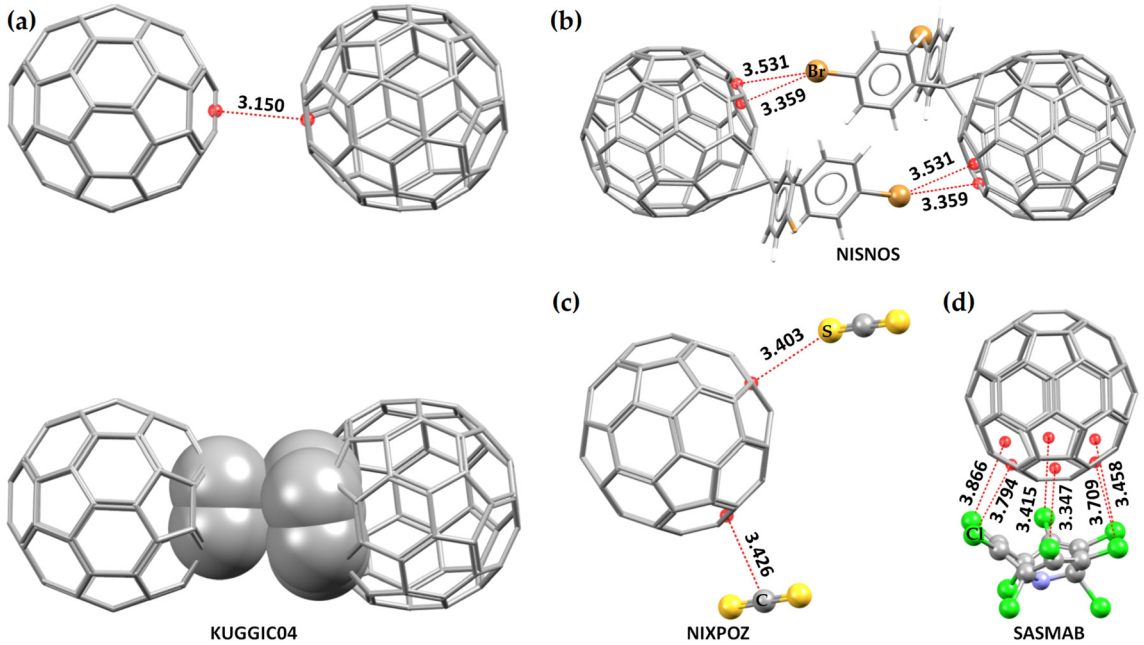


Fig. 5 Illustration of binary arrangement between interacting units found in the crystals of (a) C_{60}-Fullerene tetrakis(dimethylamino)ethylene [C_{60}, $C_{10}H_{24}N_4$];[96] (b) bis(4,4′-bromophenyl)-61,61-diylmethano C_{60} fullerene [$C_{73}H_8Br_2$];[97] (c) C_{60} fullerene tetramethyltetraselenafulvalene carbon disulfide solvate [C_{60}, $C_{10}H_{12}Se_4$,2(CS_2)];[98] the diselenyl moiety is omitted for clarity; (d) perchloroazatriquinacene C_{60}-fullerene (C_{60}·C_9Cl_9N).[99] The CSD ref. codes in uppercase letters are given in each case.

A view of these contacts is shown in Fig. 5d. These close contacts are no other than tetrel bonds. They are the result of a coulombic engagement between the negative lateral portions of the covalently bonded Cl atoms and the positive π-moiety localized at the center of the C_5 and C_6 rings of C_{60}, yet the charge transfer interactions between the frontier orbitals of the interacting moities should play an important role.

Three further systems featuring tetrel bonding are shown in Fig. 6. The crystal structure of C_{60}-fullerene hexaethylbenzene,[100] Fig. 6a, shows that hexaethylbenzene forms a base-like structure for C_{60}. The crystal is stabilized by attraction between the electrophiles on methyl H of hexaethylbenzene and the negative π-density on the surfaces of the (C═C) bonds of the C_{60} fullerene, producing H(C)H_2···π(C═C) hydrogen bonded contacts. The distance between methyl carbon and the carbon of the π(C═C) bond involved in these hydrogen bonds, 3.439 Å, is less than the twice the vdW radius of a carbon atom, 3.54 Å (r_{vdW}(C) = 1.77 Å), and r[(H_3)C···(C═C)$_{mid\text{-}point}$] = 3.449 Å. Thus, it appears that there are three (H_3)C···π(C═C) tetrel bonds between a

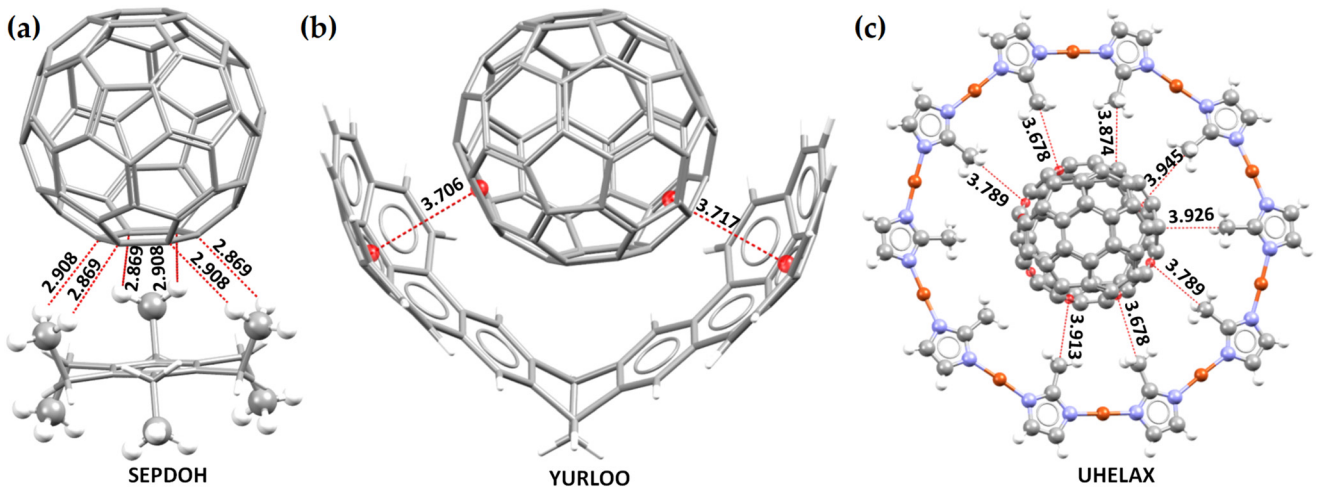


Fig. 6 The nature of the intermolecular interactions in the crystal of (a) C_{60}-fullerene hexaethylbenzene [$C_{18}H_{30}$, C_{60}];[100] (b) bis(buckycatcher II) C_{60}-fullerene [2($C_{51}H_{24}$), C_{60}];[101] (c) decakis(μ-2-methyl-imidazolato)-deca-copper(I) C_{60}-fullerene [[Cu_{10}(Mim)$_{10}$], C_{60}] (Mim = 2-methylimidazolate).[102] Selected intermolecular bond distances (Å) and CSD reference code (uppercase letters) are shown in each case. The dotted lines in red represent intermolecular interactions involved.

This journal is © The Royal Society of Chemistry 2023

pair of interacting $C_{18}H_{30}$ and C_{60} molecules that contribute to the packing arrangement in the solid state.

Concave–convex π–π interactions in the supramolecular chemistry of fullerenes with so-called "buckybowls" or "buckycatchers" are known.[101,103] For instance, the buckycatcher II, a $C_{51}H_{24}$ hydrocarbon with two corannulene pincers on a dibenzonorbornadiene tether, has an affinity for C_{60} in organic solvents. Shown in Fig. 6b is the complex between $C_{51}H_{24}$ and C_{60},[101] driven by non-covalent interactions which arise from a coulombic attraction between the C_5 rings of the two corannulene pincers that are nucleophilic (negative π-density) and the positive π-density on the interacting C_6 and C_5 rings of the C_{60} cage. One such interaction is marked in Fig. 6b, with $r(\pi\cdots\pi) = 3.71$ Å.

In the crystal structure of $[Cu_{10}(Mim)_{10}, C_{60}]$ (Mim = 2-methylimidazolate), Fig. 6c, the fullerene C_{60} molecule is caged inside the $[Cu_{10}(Mim)_{10}]$ macrocyclic host.[102] The packing between them arises from two major close contact types, $(H_3)C\cdots\pi(C{=}C)$ tetrel bonds and $C{-}H\cdots\pi(C{=}C)$ hydrogen bonds. The methyl groups in the 2-methylimidazolate units of $[Cu_{10}(Mim)_{10}]$ point toward the mid-point of their nearest C_5 or C_6 rings of C_{60}, which are nucleophilic. This conclusion is different to that of the authors of the study who claimed they could identify 30 $C{-}H\cdots\pi$ interactions between the $[Cu_{10}(Mim)_{10}]$ (Mim = 2-methylimidazolate) disk and the guest C_{60} (or C_{70}) surfaces that lead to the observed host–guest complex. That study did not clarify whether or not the formation of 30 $C{-}H\cdots\pi$ hydrogen bonds is the result of attraction of the electrophilic methyl hydrogen and the (positive or negative) π-density localized around the central region of the C_5 or C_6 rings. Our analysis suggests that the attraction occurs between the methyl hydrogen and the negative π-density distributed on the surfaces of the C=C bonding frameworks of the C_5 and C_6 rings of C_{60} (or C_{70}).

The C_{70} molecule and its implication in crystals. The polytope C_{70} molecule has D_{5h} symmetry. It has 37 faces consisting of 25 C_6 rings and 12 C_5 rings, with a carbon atom at the apex and bonds along the edges of each polygon. As found for C_{60}, QTAIM gave δ values in the ranges 1.11–1.13 and 1.11–1.39 for the C=C bonds of the C_5 and C_6 rings, respectively, indicating that the extent of electron delocalization within the carbon skeleton of the C_5 rings is different to that in the C_6 rings. The MESP analysis suggests that the reactivity of the cage's interior and exterior surfaces should be different. The nature of the electrostatic surface of the exterior of C_{70} is shown in Fig. 7. As can be seen, the surface of the central region of each C_5 or C_6 ring is more electrophilic ($V_{S,max} \gg 0$) than the C=C bond regions. Ten, ten, and five of the hexagonal C_6 rings have a $V_{S,max}$ of 10.4, 9.5, and 7.0 kcal mol^{-1}, respectively. Of the 12 C_5 rings, ten and two rings have $V_{S,max}$ = 8.2 and 9.2 kcal mol^{-1}, respectively; the last two are along the extension of the C_5 axis. The C=C bonds responsible for the C_5 or C_6 rings are having $V_{S,min}$ values range between 0.50 and −0.99 kcal mol^{-1}. However, the interior of the C_{70} cage is more electrophilic than the exterior; the largest $V_{S,max}$ values around the central regions of the interior framework of the C_5 and C_6 rings are in the range 21.0–22.5 kcal mol^{-1}, and the $V_{S,min}$ values around interior C=C bonds of the majority of these rings were also positive ($V_{S,min}$ ~18.2 kcal mol^{-1}). This may explain why the cage interior is an effective catalyst for proton transfer reactions between small molecules.[104]

Three examples, of the many deposited in the CSD, containing C_{70} are shown in Fig. 8. In them, the outer surface of C_{70} forms tetrel bonds with partners with which it interacts. The tetrel bonds in the crystal of C_{70}-fullerene bis(octa-sulfur)[105] are the $C_6(\pi)\cdots S$ and $C_5(\pi)\cdots S$ close contacts, Fig. 8a; those in $[C_{70}H_{42}, C_{70}]$,[106] Fig. 8b, are the $C_6(\pi)\cdots\pi(C_6)$ and $C_5(\pi)\cdots\pi(C_6)$ close contacts. The C_5 and C_6 surfaces of C_{70} comprise electrophilic regions (positive π-density) that are in attractive engagement with the lone-pair electron density on S in S_8, Fig. 8a, and with the negative π-density delocalized on the aromatic surfaces of the cycloarylene host (Fig. 8b).

$[C_{70}, 3(CS_2)]$, Fig. 8c, is a C_{70} based crystal system of the family of crystalline solvates, such as $[C_{90}, (CS_2)]$ and $[2(C_{70})\cdot(3CS_2)]$, of nanotubular fullerenes.[107] In $[C_{70}, (3CS_2)]$, the CS_2 molecules form chains that snake between the fullerenes

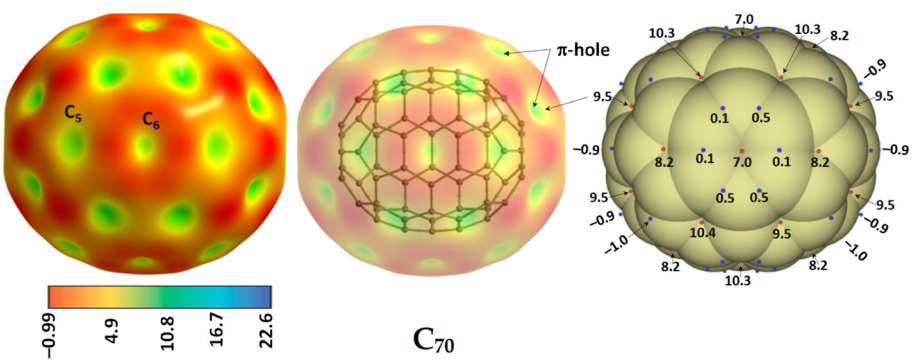


Fig. 7 The electrostatic surface plot of the C_{70} molecule mapped with the 0.001 a.u. isoelectronic density envelope, obtained with ωB97X-D/cc-pVTZ. Two different views are shown for each case (left), with the values in the color bar in kcal mol^{-1}. An approximate van der Waals surface is shown for case (right), with the local most minima and maxima ($V_{S,min}$ and $V_{S,max}$, kcal mol^{-1}) are depicted as tiny circles in blue and red, respectively.

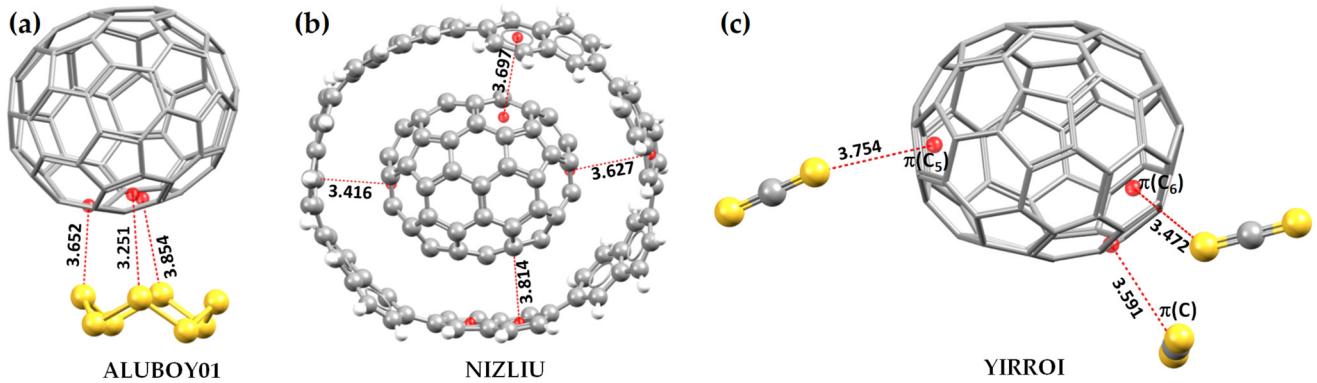


Fig. 8 Molecular models illustrating intermolecular tetrel bonded interactions between interacting partners in the crystals of (a) C_{70}-fullerene bis(octa-sulfur); (b) [$C_{70}H_{42}$, C_{70}]; (c) C_{70}-fullerene carbon disulfide solvate [C_{70}, 3(CS_2)]. Selected intermolecular close contact distances are shown in each case, together with the CSD ref. code (uppercase letters).

along the crystallographic *a*-axis. A closer look at the local arrangement between the C_{70} and three units of CS_2, Fig. 8c, shows that tetrel bonding play a vital role the packing of these molecules in the crystal. They are primarily $C_6(\pi)\cdots S$, $C_5(\pi)\cdots S$ and $S_2C(\pi)\cdots\pi(C{=}C)$ close contacts. The intermolecular distances associated with these contacts are slightly longer than the sum of the van der Waal radii of C and S atomic basins, 3.66 Å (r_{vdW}(C) = 1.77 Å and r_{vdW}(S) = 1.89 Å).

Electrostatic surfaces of graphene and its allotrope

Various 2D structures of graphene (such as honeycomb and armchair) are known.[108] We have examined two models. The MESP plot of our graphene models with and without terminal hydrogen atoms (comprising of 66 and 48 atoms) are shown in Fig. 9a and b, respectively. The major difference between the two systems is that the C_6 rings at the edge of the molecular graph in Fig. 9b are highly deformed, with curved bond paths between the bonded carbon atoms; that is not the case for $C_{48}H_{18}$ due to the terminated hydrogen atoms at the edges which stabilize the system. Therefore, the electron density distribution on the electrostatic surfaces is very different in the two models. Accordingly, the C_6 rings of H-terminated graphene molecule are nucleophilic, whereas those of the same system without terminal hydrogens are electrophilic. The former is evidenced by the negative values

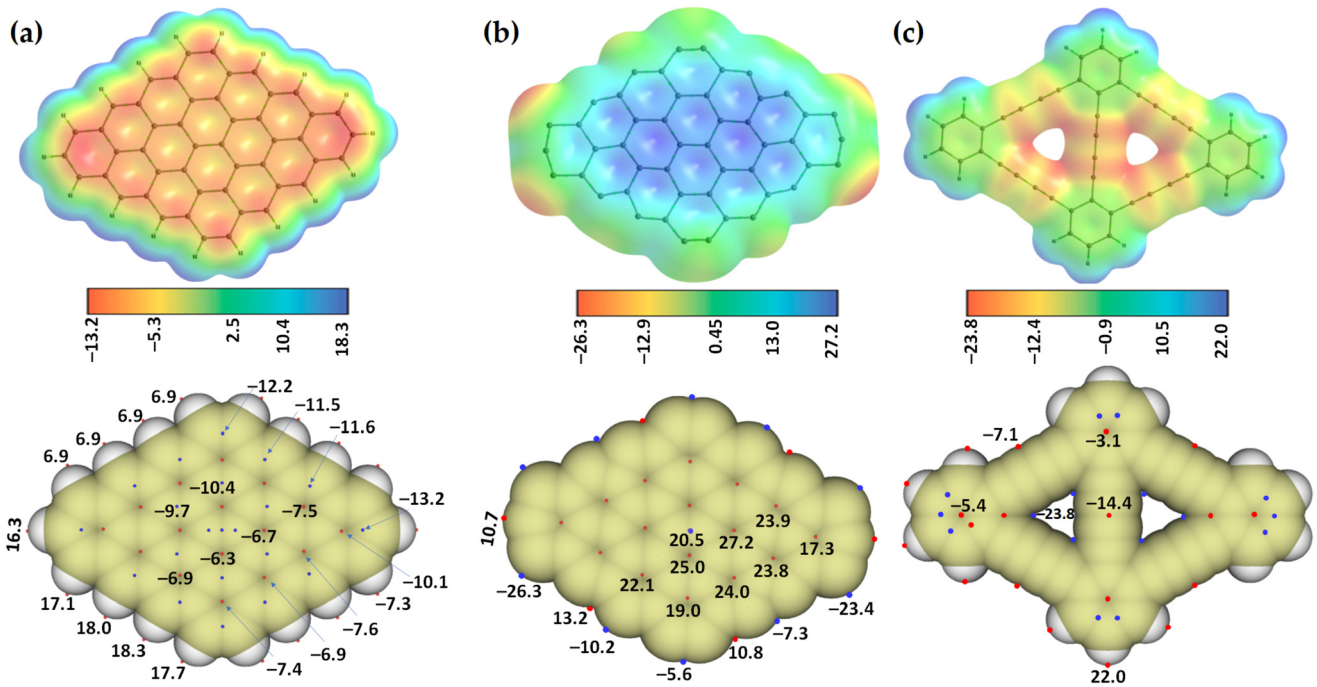


Fig. 9 (Top) The electrostatic surface of a) $C_{48}H_{18}$, b) C_{48} and c) $C_{44}H_{14}$ mapped with their corresponding 0.001 au isoelectron density envelopes, computed using ωB97X-d/cc-pVTZ. The local most maxima and minima of potential ($V_{S,max}$ and $V_{S,min}$) are represented by tiny circles in red and blue, respectively. (Bottom) Values of potential (kcal mol^{-1}) for selected maxima and minima are shown on the space-filling model of the corresponding systems that approximate the van der Waals surface.

 This journal is © The Royal Society of Chemistry 2023

of both $V_{S,max}$ and $V_{S,min}$, whereas the latter is evidenced by positive $V_{S,max}$.

Our result for the H-terminated graphene model is consistent with the results of Liang *et al.*,[109] who examined the local charge distributions in round, rectangular, and hexagonal graphene sheets. They observed that the charge distribution on the carbon atoms in these sheets is not uniform, and that at the graphene edge is strongly related to their surrounding bonds, presumably because the aromatic nature of the carbon rings is greatly distorted. In particular, Zdetsis *et al.*[110] observed that for finite nanographene(s), aromaticity patterns change periodically by addition or removal of one set of peripheral rings, which for hexagonal samples is equivalent to exchanging aromatic and nonaromatic rings, resulting in alternating $(4n + 2)$ and $4n\pi$ electron numbers, characterized, respectively, as "aromatic" and "anti-aromatic" according to Huckel's $(4n + 2)\pi$ electron rule. For infinite graphene, this interchange occurs naturally, resulting in a uniform pattern; this is probably reflected in the $C_{48}H_{18}$ model (Fig. 9a). While there is a long-standing debate on the aromaticity of graphene,[111,112] our analysis of the delocalization index alone may not be sufficient to reveal the aromatic nature of the C_6 rings. Nevertheless, the MESP model unequivocally demonstrates that a finite sized graphene-sheet with H-termination has C_6 regions that may act as acceptors of electrophiles (Fig. 9a), whereas that without H-caps has C_6 regions that may act as tetrel bond donors (Fig. 9b).

Other allotropes of two-dimensional carbon materials are graphynes, and graphdiynes. They also have a honeycomb structure.[113,114] The first, with carbon triple bonds, has been described as an hexagonal carbon network with versatile Dirac cones[115] and the second has a bandgap that widens its application in semiconductor science and technology.[113,114,116] The structure of H-terminated graphdiyne is probably not known, but analogous structures such as 1,2 : 7,8 : 13,14 : 19,20-tetrabenzocyclotetracosa-1,7,13,19-tetraene-3,5,9,11,15,17,21,23-octayne (CSD ref. code HEGGOP[117]) have been reported. The molecular graph of a 2 × 2 × 1 flat H-terminated graphdiyne, superimposed on the MESP plot, is shown in Fig. 9c. The structure of the system is built up by carbon–carbon single- and triple-bonds with the characteristic hexagons of graphene connected by diacetylenic linkages with triangular pores. Other than the electrostatic surfaces of the H atoms that are highly electrophilic ($V_{S,max}$ between 18.4 and 22.0 kcal mol^{-1}), the remaining part of the molecule is nucleophilic ($V_{S,max}$ and $V_{S,min}$ vary between −3.2 and −23.8 kcal mol^{-1}). However, it should be kept in mind that the pattern of charge density distribution should be different in an infinite crystal of graphdiyne that does not have the terminal hydrogen atoms.

Electrostatic surfaces of carbon nanotubes as tetrel bond donors

Single-walled carbon nanotubes (SWCNTs) are allotropes of carbon. They are formed when graphene sheets are seamlessly rolled into tubes with closed or open ends. Therefore, their shapes are intermediate between that of a fullerene cage and planar graphene. CNTs with different chirality show different electrical properties.[118–120]

We built models of a few CNTs with different chirality parameters, including (3, 0), (4, 0), (5, 0), (3, 3), (4, 4), (5, 5), (1, 2), and (2, 3), using the packages TubeGen 3.4 (ref. 121) and Avogadro.[122] For convenience they will be referred to by their chirality parameters.

The MESP plot of nanotube (3, 0), Fig. 10a, shows that the centroid region of the each of the four C_5 rings is positive, $V_{S,max}$ = 15.2 kcal mol^{-1}, while the remaining two C_5 rings are also positive but with $V_{S,max}$ = 7.3 kcal mol^{-1}. The C–C bond common to two nearest C_5 rings of the system has $V_{S,max}$ = 18.2 kcal mol^{-1}. However, the two terminal C atoms of each of the two C_3 rings are negative ($V_{S,min}$ = −12.7 kcal mol^{-1}), and the remaining minima found around the mid-points of the C–C bonds of the C_5 rings are all positive ($V_{S,min}$ 3.1 or 6.5 kcal mol^{-1}). An analysis of the delocalization index suggests that none of the C_5 rings possess aromatic character since δ for the C–C bonds are different; three of them have δ values between 1.244 and 1.287, implying double bond character, whereas that for the two remaining C–C bonds are between 0.880 and 1.015, indicative of single bond character. Similarly, δ for one and two C–C bonds of the C_3 rings were 0.880 and 1.287, respectively, again indicative on the non-aromatic character of these rings. These results signify that the central portion of the nanotube (3, 0) can act as a tetrel bond donor and the terminal portion as tetrel bond acceptor.

Nanotube (4, 0), Fig. 10b, contains 16 carbon atoms. The QTAIM results show there are eight similar C_5 rings and two non-equivalent C_4 rings in the molecule. The C–C bonds in the C_5 have δ values between 1.103 and 1.317. The δ for each C–C bond in one C_4 ring is 1.127 and that in the other is 1.085, indicating that these bonds may have semi-double bonded character. The MESP gave $V_{S,min}$ = −3.1 kcal mol^{-1} on the surface around the mid-points of the C–C bonds in the C_4 ring that has more delocalized electron density (see top of Fig. 10b). The equivalent points on the other C_4 ring have $V_{S,min}$ = 1.8 kcal mol^{-1}. The centroid regions of the these rings have $V_{S,max}$ of 4.9 and 6.2 kcal mol^{-1}, respectively, showing that the electrostatic surface of the latter ring is entirely electrophilic. While there are six C_5 rings in nanotube (4, 0), the central portions of the upper four are weakly electrophilic while the bottom four shown in Fig. 10b have $V_{S,max}$ 9.9 and 16.2 kcal mol^{-1}. Moreover, the carbon atom common to three nearest C_5 rings has the highest electrophilicity, with $V_{S,max}$ = 16.8 kcal mol^{-1}. These positive regions are than tetrel-centered π-holes.

Nanotube (5, 0), Fig. 10c, comprises 12 pentagons. The central surface of all of them is positive, with the strength of the π-holes varying from 7.8 to 11.0 kcal mol^{-1}. The surfaces of six C–C bonds that share edges with six C_5 rings are nucleophilic with $V_{S,min}$ = −5.2 kcal mol^{-1}. The δ values of the C–C bonds in the C_5 rings range between 0.995–1.384, showing that some possess single bond character while

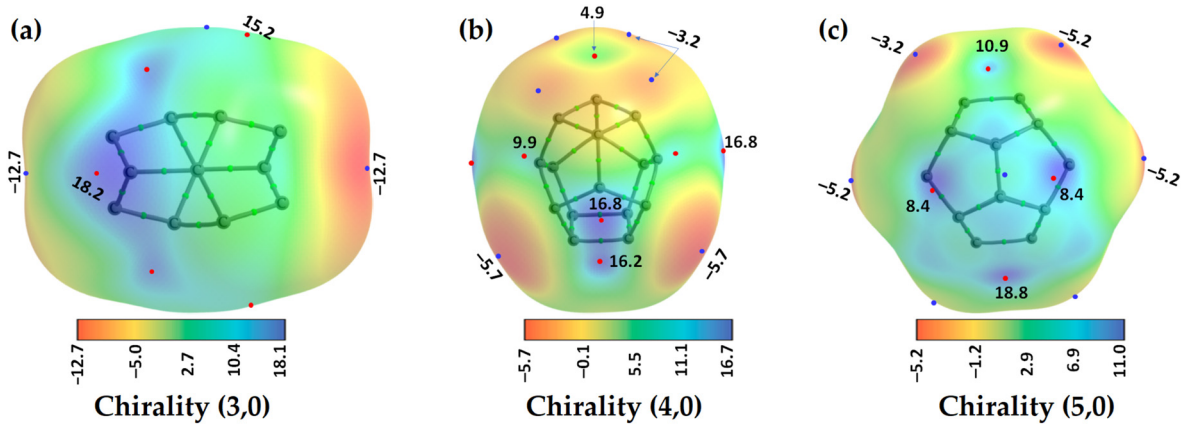


Fig. 10 The electrostatic surfaces of nanotubes mapped with their corresponding 0.001 a.u. isoelectron density envelopes, with chirality (a) (3, 0), (b) (4, 0) and (c) (5, 0), obtained with ωB97X-D/cc-pVTZ. The local most minima and maxima ($V_{S,min}$ and $V_{S,max}$), are depicted as tiny circles in blue and red, respectively, and values are in kcal mol^{-1}.

others have double bond character. From the MESP results, it seems that the surface of nanotube (5, 0) acts both as a π-hole acceptor and donor, but with the former more predominant than the latter.

The superimposed molecular graphs and MESP for nanotubes with chirality (1, 2) and (2, 3) are shown in Fig. 11a and b, respectively. Their electrostatic surfaces are very different to each other. The surface of the central carbon framework of the (1, 2) is composed of negative and positive regions, as is the surface of the end potions (MESP values with color bar in Fig. 2a bottom). The most nucleophilic region on the surface of the system is identified on the surface of the C═C bonds that have largest delocalization index, with δ = 1.67. However, because of the curved nature of several C–C bonds and the irregular shape of the nanotube, the distribution of charge density on the surface of the nanotube is non-uniform, evidenced by values of δ that vary between 0.54 and 1.67.

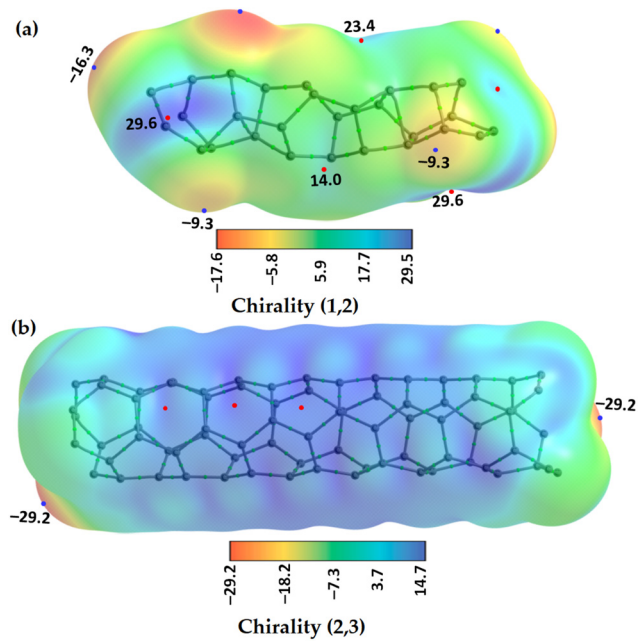


Fig. 11 The electrostatic surfaces of open-ended nanotubes with their corresponding 0.001 a.u. isoelectronic density envelopes, with chirality (a) (1, 2) and (b) (2, 3), obtained with ωB97X-D/cc-pVTZ. Selected local most minima and maxima ($V_{S,min}$ and $V_{S,max}$), are depicted as tiny circles in blue and red, respectively, and values are in kcal mol^{-1}.

The electrostatic surface of nanotube (2, 3) is very different. A large part of it is purely electrophilic with $V_{S,min} > 0$ and $V_{S,max} > 0$. Specifically, the $V_{S,min}$ values on the C═C bonding regions in the central position range between 4.7 and 11.3 kcal mol^{-1} and the $V_{S,max}$ values around the centroid regions of the C_6 rings vary between 4.8 and 14.7 kcal mol^{-1}. There are two specific surface regions that lie at the open ends of the C═C bonds that are largely nucleophilic ($V_{S,min}$ = −29.2 kcal mol^{-1}). The underlying reason is that these C═C bonds are strained, and are associated with delocalization indices close to 2.2, indicative of bonds between C atoms with some sp character, and with relatively large electron density on their surfaces. By contrast, the CC bonds in the central portions of the nanotube δ varies between 1.10 and 1.35.

Nanorings have been known for some time.[123–125] The structures shown in Fig. 12 have chirality (3, 3), (4, 4) and (5, 5). Each can be imagined a ring-structure with a torus-like van der Waals surface. The outer electrostatic surface of the carbon atoms of the ring with chirality (3, 3), Fig. 12a, which is orthogonal to the C═C bonding direction, is entirely electrophilic ($V_{S,max}$ = 13.1 kcal mol^{-1}), whereas that of the C═C bonds is nucleophilic ($V_{S,min}$ = −8.6 kcal mol^{-1}).

When the diameter of the carbon ring becomes larger, with chirality (4, 4) and (5, 5) (Fig. 12b and c, respectively), the charge density is segmented into belt-like positive and negative regions. The most positive and negative regions ($V_{S,max}$ = 9.4 (8.7) kcal mol^{-1} and $V_{S,min}$ = −2.5 (or −1.8) kcal mol^{-1}, respectively) on these two ring systems show up on the outer surface of each carbon atom, and the mid-point of each C═C bond, respectively, indicating that these can act as tetrel bond donors and acceptors of electrophiles, respectively. A very similar feature is observed for the interior surfaces of these rings. The

 This journal is © The Royal Society of Chemistry 2023

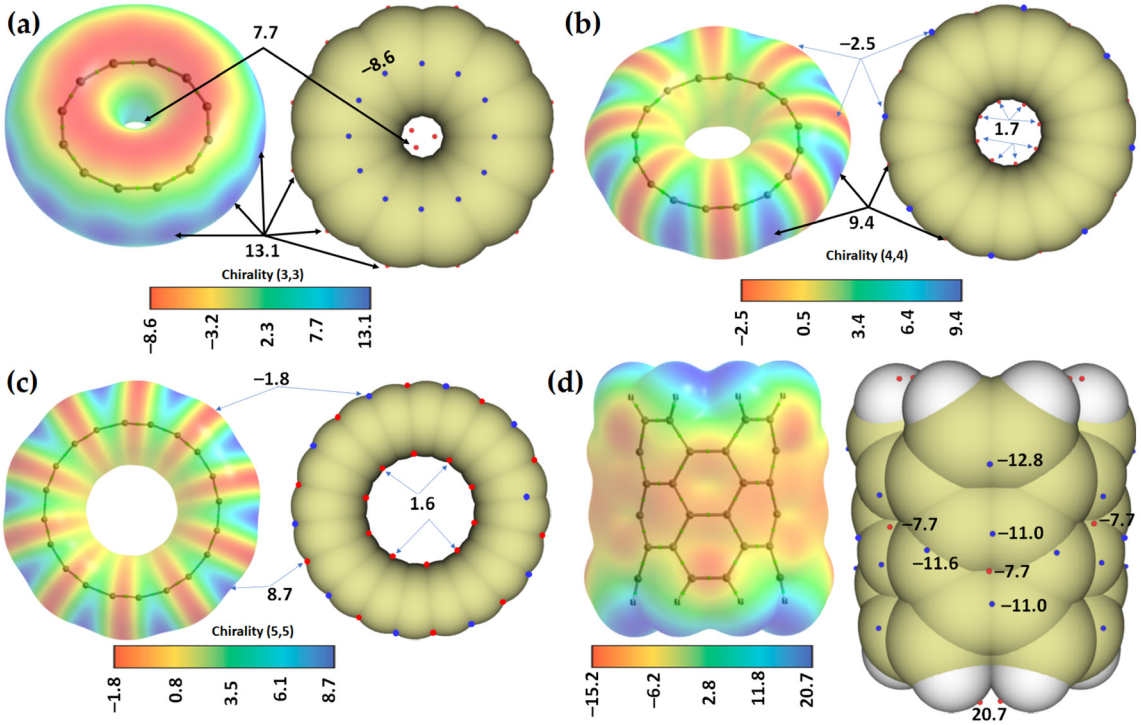


Fig. 12 The electrostatic surfaces of nanorings with their corresponding 0.001 a.u. isoelectron density envelopes, with chirality (a) (3, 3), (b) (4, 4) and (c) (5, 5), obtained with ωB97X-D/cc-pVTZ. Shown in (d) is the nanotube with chirality (5, 5) and length 3.0 (periodic unit). The local most minima and maxima ($V_{S,min}$ and $V_{S,max}$), are depicted as tiny circles in blue and red, respectively, and values are in kcal mol^{-1}.

positive regions are described by the local most maxima of potential when mapped on the 0.001 au isoelectron density surface ($V_{S,max}$ = 1.7 kcal mol^{-1} in Fig. 12b and $V_{S,max}$ = 1.6 kcal mol^{-1} in Fig. 12c). However, the local most minima were not observed using this envelope; they only appeared when a higher isodensity envelope, such as 0.0015 au, was used. For instance, the $V_{S,max}$ ($V_{S,min}$) values mapped on this envelope were 11.2 and 3.1 (−1.7 and 1.2) kcal mol^{-1} on the outer and inner portions of the ring shown in Fig. 12c, respectively.

The molecular graph of a hydrogen-capped single-walled carbon nanotube (SWCNT) with chirality (4, 4) and length 3.0 (periodic units) is shown in Fig. 12d. Because of the presence of terminal H atoms, there are regions of rich electron density and regions of poor electron density, similar to what is expected for benzene. In other words, the aromatic part of the nanotube (the central region) is nucleophilic, while the surface region dominated by H atoms is electrophilic. Of course, the nature of this electron density distribution can be changed when all H atoms are removed, as was in graphene sheets (*vide supra*). From Fig. 12d, it is clear that both the centroid of the C_6 rings ($V_{S,max}$ = −7.7 kcal mol^{-1}) and the C–C bonding region ($V_{S,min}$ between −11.0 and −12.8 kcal mol^{-1}) on the nanotube's outer surface are largely nucleophilic. The interior of the carbon backbone of the nanotube is also nucleophilic, with the corresponding regions having $V_{S,max}$ = −3.7 kcal mol^{-1} and $V_{S,min}$ = −15.2 kcal mol^{-1}, respectively The delocalization index δ for the C–H bonds is <1 (δ = 0.948) and that for the C–C pair is >1 (δ between 1.081 and 1.41). Thus, the atom–atom pairs responsible for the carbon backbone of the nanotube have large δ and hence possess relatively large nucleophilicity.

End-capped polycyclic aromatic hydrocarbons have attracted much attention.[126,127] The crystal of the C_{50} fullerene carbon disulfide system $[C_{50}H_{10}\cdot(CS_2)_2]$ is an example.[128] The nature of endohedral and exohedral interactions between the building blocks of the system can be seen in Fig. 13a and b, respectively. The geodesic polyarene is a short close-ended hemispherical (5, 5) CNT with single-chirality (Fig. 14).

The (outer) exohedral surface of the centroid region of each of the six C_5 rings of the nanotube has $V_{S,max}$ = 1.1 kcal mol^{-1}; these regions are therefore weakly electrophilic. Similarly, the centroid region of each of the five C_6 rings responsible for the central nanotube around the end-capped C_5 ring is weakly electrophilic ($V_{S,max}$ = 1.9 kcal mol^{-1}), whereas those are close to the open-ended CNT without H-termination have $V_{S,max}$ = 0.6 kcal mol^{-1}. However, the centroid region of the remaining C_6 rings near the open-ended portion of the CNT with H-caps is nucleophilic ($V_{S,max}$ = −3.9 kcal mol^{-1}). The surfaces around the C=C bonding regions of the C_5 and C_6 rings are nucleophilic, with $V_{S,min}$ values between −6.3 and −7.9 kcal mol^{-1}. On the other hand, the inner (endohedral) part of the CNT is relatively more electrophilic. The $(C_5)_\pi\cdots S$ type endohedral tetrel bonding shown in Fig. 13a occurs between S of CS_2 and the central portion of the C_5 ring of the CNT. It is a result of columbic attraction between sites of opposite electrostatic potential localized between the interacting regions since the surface of

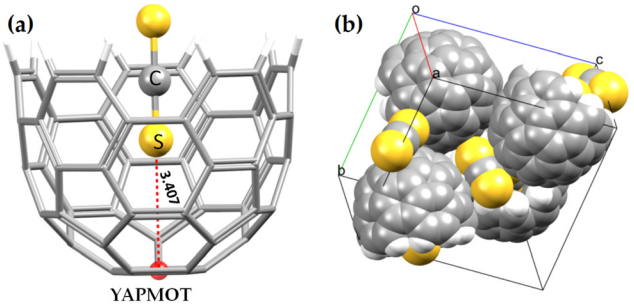


Fig. 13 a) The nature of endohedral link between the building blocks in the crystal of C_{50} fullerene carbon disulfide, showing the formation of a tetrel bond between negative (lone-pair) S of CS_2 and the positive π-density at the centroid region of the C_5 ring of $C_{50}H_{10}$. b) Space-filling model of the unit-cell of the crystal, comprising other types of tetrel bonds (not marked) such $(S_2)C\cdots\pi(C{=}C)$ and $(SC)S\cdots\pi(C_6)$. Atom labeling is shown in (a). Selected $(SC)S\cdots\pi(C_5)$ bond distance in Å. The CSD reference code is depicted in uppercase letters.

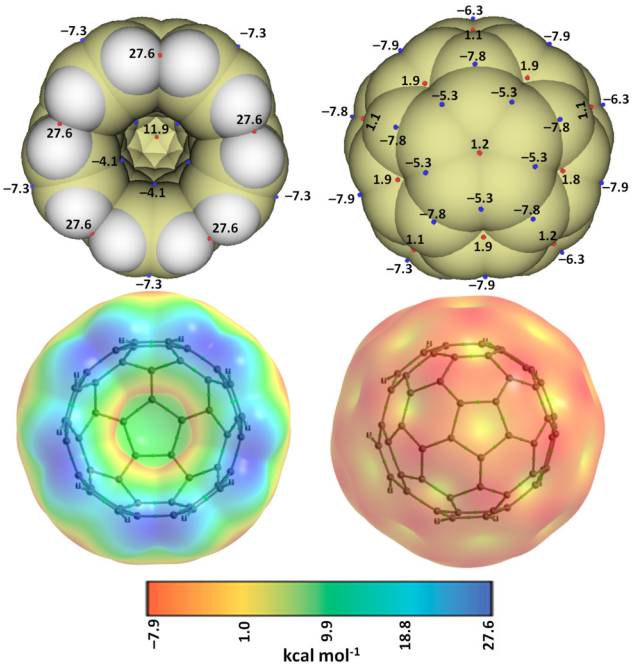


Fig. 14 The electrostatic surface plot of $C_{50}H_{10}$ carbon nanotube, mapped with the 0.001 a.u. isoelectronic density envelope, obtained with [ωB97X-D/cc-pVTZ]. (Top) Selected $V_{s,max}$ and V_{max} values (kcal mol^{-1}) are shown on the van der Waals surface the CNT; (Bottom) the color coded MESP of $C_{50}H_{10}$. (Left) The H-terminated open-ended portion of the $C_{50}H_{10}$ CNT faces the viewer. (Right) The closed-ended C_5 ring of the $C_{50}H_{10}$ CNT faces the viewer.

the C_5 ring is strongly positive ($V_{S,max}$ = 11.9 kcal mol^{-1}) and attracts the negative (lone-pair dominated) portion of S. Other possible tetrel bonded interactions between the building blocks responsible for the crystal include $(C_6)_\pi\cdots S$ and $(S_2)C\cdots\pi(C{=}C)$. The most favorable electrophilic sites are associated with the open-ended (H-terminated) portion of the CNT that are in attractive engagement with the negative site on S, forming C–H···S hydrogen bonds, as seen in the unit-cell of the crystal shown in Fig. 13b.

Further examples of crystals driven by tetrel bonds and other non-covalent interactions

Two different views (ball-and-stick and space-filling) of a chemical model describing the complexation of C_{60} with a conical region of a nanometer-sized geodesic phenylene bowl[129] are shown in Fig. 15. The attraction between the interacting moieties in the ball-in-bowl structure can be rationalized by the MESP model of the C_{60} (Fig. 12), and the phenylene bowl. Although we did not compute the MESP of the latter, we can speculate that the H-sites in the arene moieties and the five C_6 rings in the central portion of the phenylene bowl are electrophilic and nucleophilic, respectively, as was calculated for H-terminated graphene/graphdiyne (Fig. 9a/c), or H-capped nanotube (Fig. 12d). Also, from Fig. 12, it is obvious that the surfaces of the centroid portion of the C_6 ring of the C_{60} molecule resting on the phenylene bowl (Fig. 15, left) is electrophilic, and the C=C bonds forming this ring is nucleophilic. The latter negative regions on the surface of the C=C bonds are in attractive engagement with some of the nearby strongly electrophilic H-sites of the phenylene bowl (interacting H atoms marked yellow, Fig. 6, left), forming C–H···π(C=C) hydrogen bonds. Similarly, the central portion of the C_4H_2 ring (marked yellow in Fig. 6(left)) of the phenylene bowl can be expected to be nucleophilic, as observed for the $C_{50}H_{10}$ CNT system (Fig. 5), which is in attractive engagement with the electrophilic C_6 centroid region (π-hole centered tetrel bond donor) of the fullerene C_{60}, thus forming C_6(π-hole)···π tetrel bonded interactions. There are also C_6(π-hole)···π(C_6) interactions between the C_6 rings of the bowl and C_{60} (marked blue and green in Fig. 15, respectively, left). Because of these specific arrangements between the interacting units, as well as other similar interactions, the centroid of the C_6 ring of C_{60} facing the phenylene bowl does not coincide with centroid of the H-terminated ring (marked yellow on left of Fig. 15) of the phenylene bowl.

Systems where the fullerene balls are nestled within a nanotube are colloquially referred to as nanoscopic peapods.[130] They have tunable electronic properties, with a concave–convex interface. It has been suggested that assembly is driven solely by van der Waals interactions,[131,132]

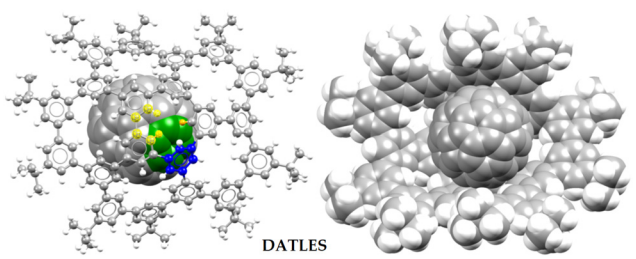


Fig. 15 Two different views of the 1 : 1 arrangement between fullerene C_{60} and the conical region of a nanometer-sized geodesic phenylene bowl [$C_{160}H_{150}$, C_{60}]. The CSD reference the system is shown in uppercase letters. Carbon and hydrogen atoms are shown as balls in gray (and black) and white, respectively.

This journal is © The Royal Society of Chemistry 2023

but this is speculative since the π···π interactions are not always van der Waals type. Shown in Fig. 16 is the structure of a molecular peapod reported by Matsuno and coworkers,[132] composed of (*P*)-(12,8)-[4]cyclo-2,8-anthanthrenylene and fullerene C_{60}. As outlined for the ball-in-bowl system ([$C_{160}H_{150}$, C_{60}]) discussed above, we observed that, among others, two dominant types of attractive interactions drive the supramolecular assembly in the peapod. They are marked in Fig. 16a and b, consisting of C–H···π(C═C) hydrogen bonds and C_6(π-hole)···π(C═C) tetrel bonded interactions, respectively as revealed by the MESP model. The nucleophilic character of the arene framework of the anthanthrenylene engages in coulombic attraction with positive π-hole of the C_6 ring (colored pink in Fig. 16a) of C_{60} fullerene, forming C_6(π-hole)···π(C═C) tetrel bonds (marked in Fig. 16a). Similarly, the aliphatic hexyl chains at the edge of the anthanthrenylene are folded to wrap around the C_{60} molecules in the crystal. This is expected since the H atoms of the hexyl chains are highly electrophilic, and are attracted toward the sp^2-carbon networks responsible for the C═C bonds in C_{60}, which are nucleophilic (Fig. 3), resulting in the formation of C–H···π(C═C) hydrogen bonds. These interactions are marked in Fig. 16b, in which the H atoms (colored yellow) of the $–CH_2$ and $–CH_3$ fragments in the hexyl chains face the C═C bonding regions of C_{60}.

Representative carbonaceous systems both as electron density donor and acceptor systems for partner species: a case study

To demonstrate the concepts developed above, four model fullerene and nanotube systems were considered: C_{20}, C_{60}, C_{70}, and $C_{50}H_{10}$, which were treated both as electron density acceptors and donors for a number of interacting molecules. Specifically, the binary complexes of C_{20} with HX (X = F, Cl, Br), X_2 (X = F, Cl, Br), and N_2, were investigated using density functional theory and the intermolecular interactions responsible for the formation of these complexes were characterized with QTAIM, NBO and IGM-δg^{inter} analyses.

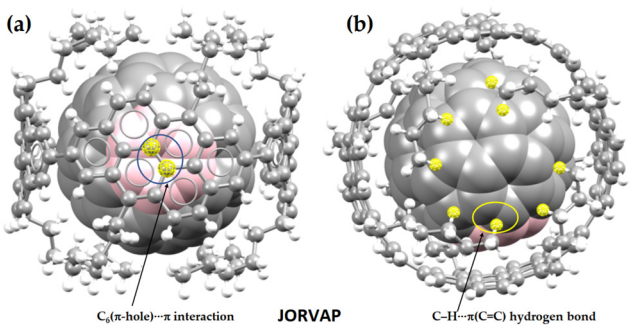


Fig. 16 (a) and (b) The ball-and-stick and space-filled model of a supramolecular complex between a tubular molecule, (*P*)-(12,8)-[4] cyclo-2,8-anthanthrenylene [$C_{136}H_{136}$], and fullerene C_{60} in the crystalline solid state (CSD ref. code JORVAP). The carbon and hydrogen atoms are shown as balls in gray (and pink/yellow) and white, respectively.

Several dimeric complexes of C_{60} and $C_{50}H_{10}$ with CS_2, as well as that of C_{70} with I_2, I_3^-, and CS_2, similar to those observed in crystals, were also considered and the intermolecular interactions between them were characterized using the same computational approaches.

The surfaces of C═C bonds in C_{20}, Fig. 1a, are nucleophilic (colored red and yellow), and the centroid of the C_5 ring is electrophilic (colored blue). The former has the ability to accept a hydrogen bond, halogen bond, or pnictogen bond, or tetrel bond, whereas the latter has the ability to donate a tetrel bond. The structures shown in Fig. 17a–c confirm that the C═C delocalized bond in a C_5 ring is an acceptor of a hydrogen bond from HX (X = F, Cl, Br), forming X–H···$(C═C)_\pi$ close contacts. Similarly, the electron density rich C_π site of the C_5 ring in C_{20} that features a negative electrostatic potential on its surface acts as a relatively strong nucleophilic gate for the electrophile on the H atom in HX, forming X–H···$(C)_\pi$ hydrogen bonds when X = F and Cl (*cf.* Fig. 17d–f). Although only a marginal transfer of the proton takes place from HX to the C atom of the C_5 ring when X = F and Cl (*cf.* Fig. 17d–f), there is a complete transfer of H from HBr to the interacting carbon of C_{20}, leading to the formation of an ion-pair [$C_{20}H^+$·Br^-]. This accords with increasing acidity order of the hydrohalic acids, HF < HCl < HBr, and is in agreement with the interaction energies shown in Table 2. This suggests that the outer surface of C_{20} may be an appropriate chemical system for the study of proton transfer reactions of small molecules, as observed for other fullerene systems.[133] The interaction energies of X–H···$(C═C)_\pi$ are smaller than the interaction energies of X–H···$(C)_\pi$ for a given X in X–H···C_{20} (Table 2).

Kawabata and Tachikawa[134] have examined the complexation of Li^+ and C_{20}. Our investigation shows that the attack of the electrophile Li^+ on the nucleophilic gates of the C_{20} fullerene system is very similar to the cases shown in Fig. 17a–f, with a binding energy of −42.36 kcal mol^{-1} for the most stable Li^+···C_{20} conformer at CAM-B3LYP/6-311+G(d). The structures in Fig. 17a–c are first order saddle points, whereas those in Fig. 17d–f are stable local minima, consistent with the corresponding conformers reported for the Li^+···C_{20} system.[134] The complexes C_{20}···H–X (X = F, Cl, and Br) and C_{20}···H_2O were also reported at the MP2/6-31+G*//B3LYP/6-31G* level of theory; two types of interactions were found: (i) very weak X–H···π H-bond interactions and (ii) long range van der Waals interactions of the H–X···C type.[135] The surface reactivity of C_{20} for the adsorption of hydrogen (including molecular H_2) has been reported elsewhere.[136]

Another set of five binary complexes of C_{20} with diatomic molecules is shown in Fig. 18a–e. In all five cases the diatomic molecules lie almost horizontally on the outer surface of a C_5 ring of C_{20}. The covalent bond of the diatomic molecule is either marginally increased or decreased on coming into close proximity of the fullerene. In all cases the lateral negative sites of the diatomic molecule are in attractive engagement with the surface of the C_5 ring. This is

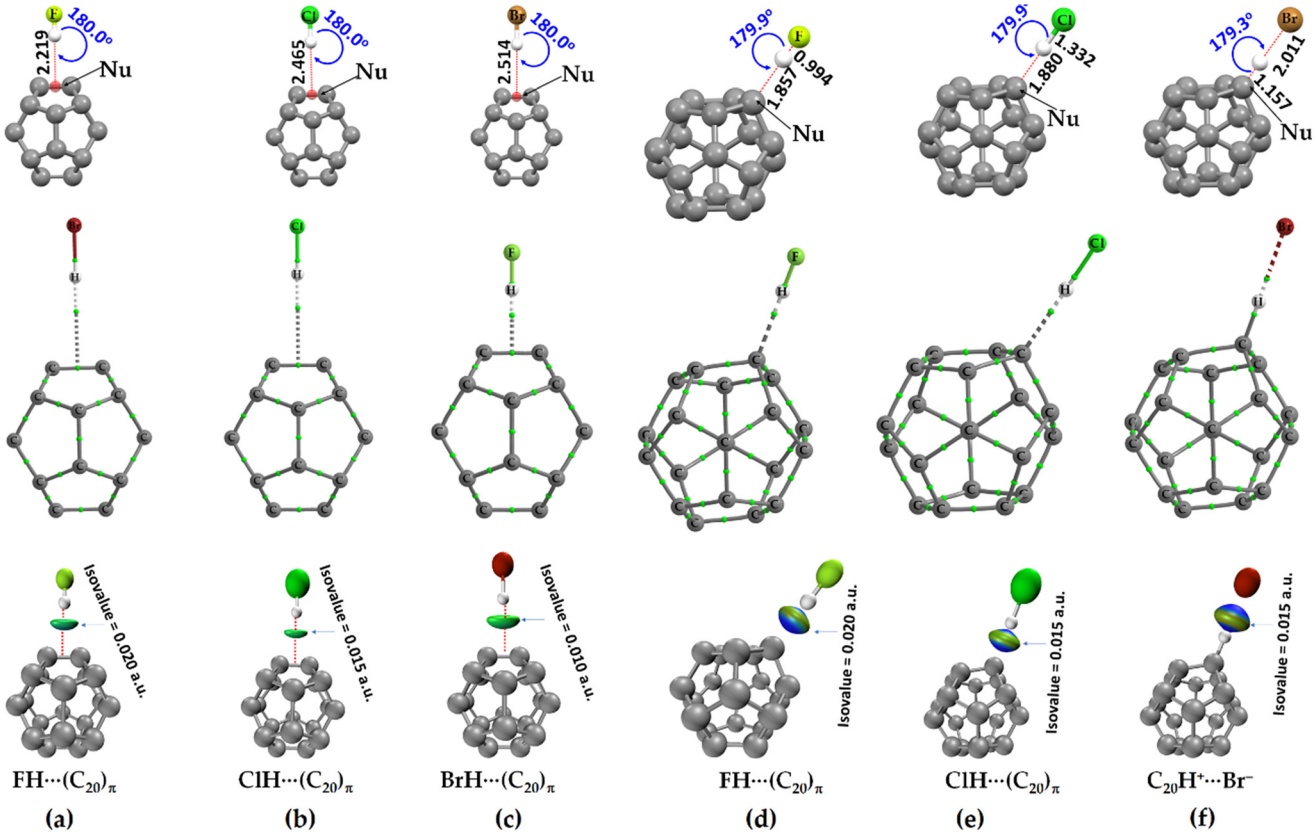


Fig. 17 The [ωB97XD/cc-pVTZ] level optimized geometry (top), molecular graph (middle) and IGM-δg^{inter} based isosurfaces (bottom) of (a) FH···C_{20}; (b) ClH···C_{20}; (c) BrH···C_{20}. Shown on (d)–(f) are the corresponding plots for the same systems with a C site as the nucleophilic gate. Selected (intermolecular) bond distances and bond angles are in Å and degrees, respectively. The bond paths and bond critical points responsible for the molecular graphs are shown as solid and dotted lines in atom color. The tiny red dots between a pair of carbon atoms of C_{20} (top) in (a)–(c) represents the bond critical point (bcp). Blue and green IGM-δg^{inter} isosurfaces signify strong and weak interactions, respectively.

Table 2 The [ωB97XD/cc-pVTZ] level interaction energies (kcal mol^{-1}) of binary complexes of some selected fullerene systems with molecules HX (X = F, Cl, Br), N_2, CO, F_2, Cl_2, Br_2, and CS_2

Fig.	System	ΔE	ΔE (BSSE)
Fig. 17a	FH···C_{20}	−4.50	−3.39
Fig. 17b	ClH···C_{20}	−2.79	−2.56
Fig. 17c	BrH···C_{20}	−2.67	−2.48
Fig. 17d	FH···C_{20}	−10.34	−9.02
Fig. 17e	ClH···C_{20}	−7.97	−7.61
Fig. 17f	$C_{20}H^+$···Br^-	−84.01	−83.18
Fig. 18a	C_{20}···N_2	−1.25	−0.88
Fig. 18b	C_{20}···CO	−1.27	−1.04
Fig. 18c	C_{20}···F_2	−1.48	−0.78
Fig. 18d	C_{20}···Cl_2	−2.04	−1.75
Fig. 18e	C_{20}···Br_2	−2.69	−2.47
Fig. 20a	C_{60}···CS_2	−1.57	−1.45
Fig. 20b	C_{60}···CS_2	−3.58	−3.32
Fig. 20c	C_{70}···CS_2	−3.70	−3.44
Fig. 20d	C_{70}···CS_2	−1.52	−1.40
Fig. 20e	C_{70}···CS_2	−1.96	−1.82
Fig. 21a	C_{70}···I_2	−4.93	−4.76
Fig. 21b	C_{70}···I_2	−4.45	−4.26
Fig. 21c	C_{60}···I_3^-	−11.49	−11.15
Fig. 22a	$C_{50}H_{10}$···CS_2	−2.07	−1.93
Fig. 22b	$C_{50}H_{10}$···CS_2	−14.31	−13.35

in agreement with the presence of a π-hole as deduced from the MESP model shown in Fig. 19a–e. While the surfaces around the mid-points of all five diatomic molecules are sites of positive electrostatic potential, the lateral negative sites on an X atom in all the three X_2 (X = F, Cl, Br) molecules form $(C_5)_{\pi\text{-hole}}$···X tetrel bonds. The negative region on lateral portion of the second X atom in X_2 is also in attractive engagement with positive potential on a C atom in C_{20}. The mid-point positive regions in these molecules are in attractive engagement with the negative $(C{=}C)_{\pi\text{-hole}}$, forming a lump–hole interaction. A similar explanation applies for the attraction between CO (or N_2) with the C_5 framework of the C_{20} fullerene, forming $(O)C_\pi\cdots(C{=}C)_{\pi\text{-hole}}$ and $C_\pi\cdots N_2$ close contacts, respectively. In addition, there may be weak counterintuitive $(C_5)_{\pi\text{-hole}}\cdots(CO)_{\pi\text{-hole}}$ $(C_5)_{\pi\text{-hole}}\cdots(N_2)_{\pi\text{-hole}}$ interactions.[137–139] These conclusions accord with the charge-density based bond path topologies between the interacting moieties, as well as with the IGM-δg^{inter} isosurfaces shown in Fig. 18a–e (middle and bottom panels, respectively).

The two complexes formed between C_{60} and CS_2 observed in the crystal of [C_{60}, $C_{10}H_{12}Se_4$, 2(CS_2)] (CSD ref: NIXPOZ)[140] were fully relaxed after removing $C_{10}H_{12}Se_4$. The results are shown in Fig. 20a and b. In Fig. 20a, the electrophilic π-hole on the C_5 ring is in coulombic attraction with the lone-pair

 This journal is © The Royal Society of Chemistry 2023

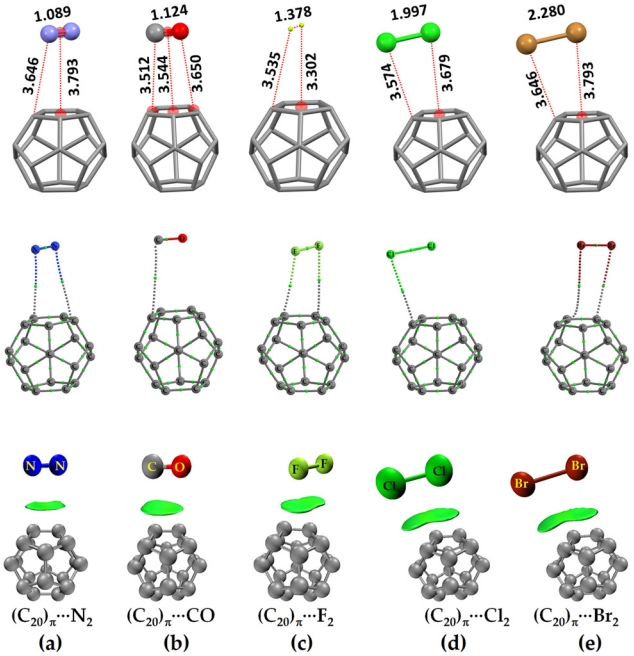


Fig. 18 The [ωB97XD/cc-pVTZ] level optimized geometry (top), molecular graph (middle) and IGM-δg^{inter} based isosurfaces (bottom) of (a) $(C_{20})_\pi\cdots N_2$; (b) $(C_{20})_\pi\cdots CO$; (c) $(C_{20})_\pi\cdots F_2$; (d) $(C_{20})_\pi\cdots Cl_2$; (e) $(C_{20})_\pi\cdots Br_2$. Selected bond distances are in Å and, the IGM-δg^{inter} isosurfaces (green volumes, bottom) were determined using a 0.005 a.u. isosurface. The bond paths and bond critical points leading to the molecular graphs are shown as solid and dotted lines in atom color. The tiny red dots within the C_5 ring in C_{20} (top) in (a)–(e) represent the centroid. Green IGM-δg^{inter} isosurfaces signifies the presence of weak interactions.

on S in CS_2, forming a $(C_5)_\pi\cdots S$ tetrel bond ($r[(C_5)_\pi\cdots S]$ = 3.570 Å). In Fig. 20b, the centroids of C_6 and C_5 rings of the C_{60} fullerene are in attractive engagement with both nucleophile on the S atoms of CS_2, thus forming $(C_6)_\pi\cdots S$, and $(C_5)_\pi\cdots S$ tetrel bonds. The electrophilic π-hole on the C═C bond is linked attractively with the nucleophile on C═C carbon framework of C_{60}, thus forming the $(S_2)C_\pi\cdots_\pi(C{=}C)$ tetrel bond. Because of many intermolecular interactions are involved, the conformation in Fig. 20b is stronger than that in Fig. 20a (see Table 2 for ΔE and ΔE (BSSE) values). The nature of the non-covalent interaction revealed by the MESP model (see MESP graphs in Fig. 3 for C_{60}) is in agreement with IGM-δg^{inter} based isosurfaces (Fig. 20 (middle)). However, QTAIM did not show $(C_6)_\pi\cdots S$, and $(C_5)_\pi\cdots S$ tetrel bonds in Fig. 20b (middle), although that was not the case for the $(S_2)C_\pi\cdots(C{=}C)_\pi$ interaction.

Illustrated in Fig. 20c–e are the relaxed geometries of three conformers of C_{70} with CS_2, a system which is also known in the crystalline phase (*cf.* Fig. 8c).[107] These are the result of an attractive engagement between two lone-pair on two S and the electrophilic π-hole (C) of CS_2 with the $(C_6)_\pi$, $(C_5)_\pi$, and nucleophilic $(C{=}C)_\pi$, forming $(C_6)_\pi\cdots S$, $(C_5)_\pi\cdots S$ and $(S_2)C_\pi\cdots(C{=}C)_\pi$ tetrel bonds, respectively. Of the three, the conformer in Fig. 20c is the more stable (*cf.* Table 2 for ΔE and ΔE (BSSE) values).

We have also examined the DFT results of two binary complexes of C_{70} with I_2 (Fig. 21a and b, respectively) and a binary complex of C60 with I_3^- (Fig. 21c), which are known in the solid state (CSD references YOVWEN[141] and PATVIQ,[142] respectively). The orientation between the interacting units in the two structures of the former system found in the crystalline phase are slightly distorted compared to those found in the gas phase. For instance, our inspection shows that an $I\cdots C_\pi$ halogen bond ($r(I\cdots C_\pi)$ = 3.104 Å and $\angle$I–I$\cdots C_\pi$

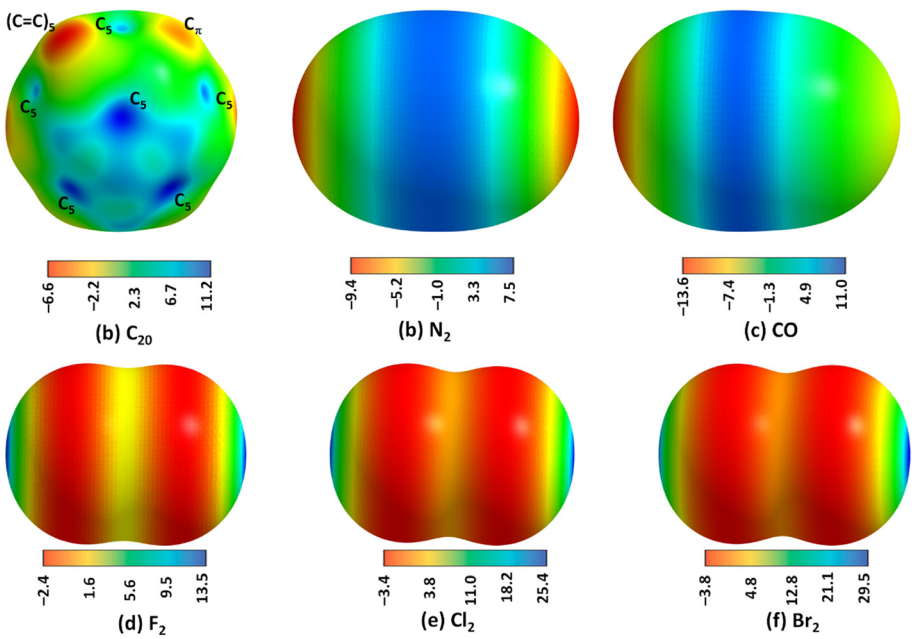


Fig. 19 The [ωB97XD/cc-pVTZ] level 0.001 a.u. isoelectron density envelope mapped potential on the electrostatic surfaces of (a) C_{20}; (b) N_2; (c) CO; (d) F_2; (e) Cl_2; and (f) Br_2. Selected C_5 and C═C, C regions are marked in (a). The local most minima and maxima ($V_{S,min}$ and $V_{S,max}$), are depicted as tiny circles in blue and red, respectively, and values are in kcal mol^{-1}.

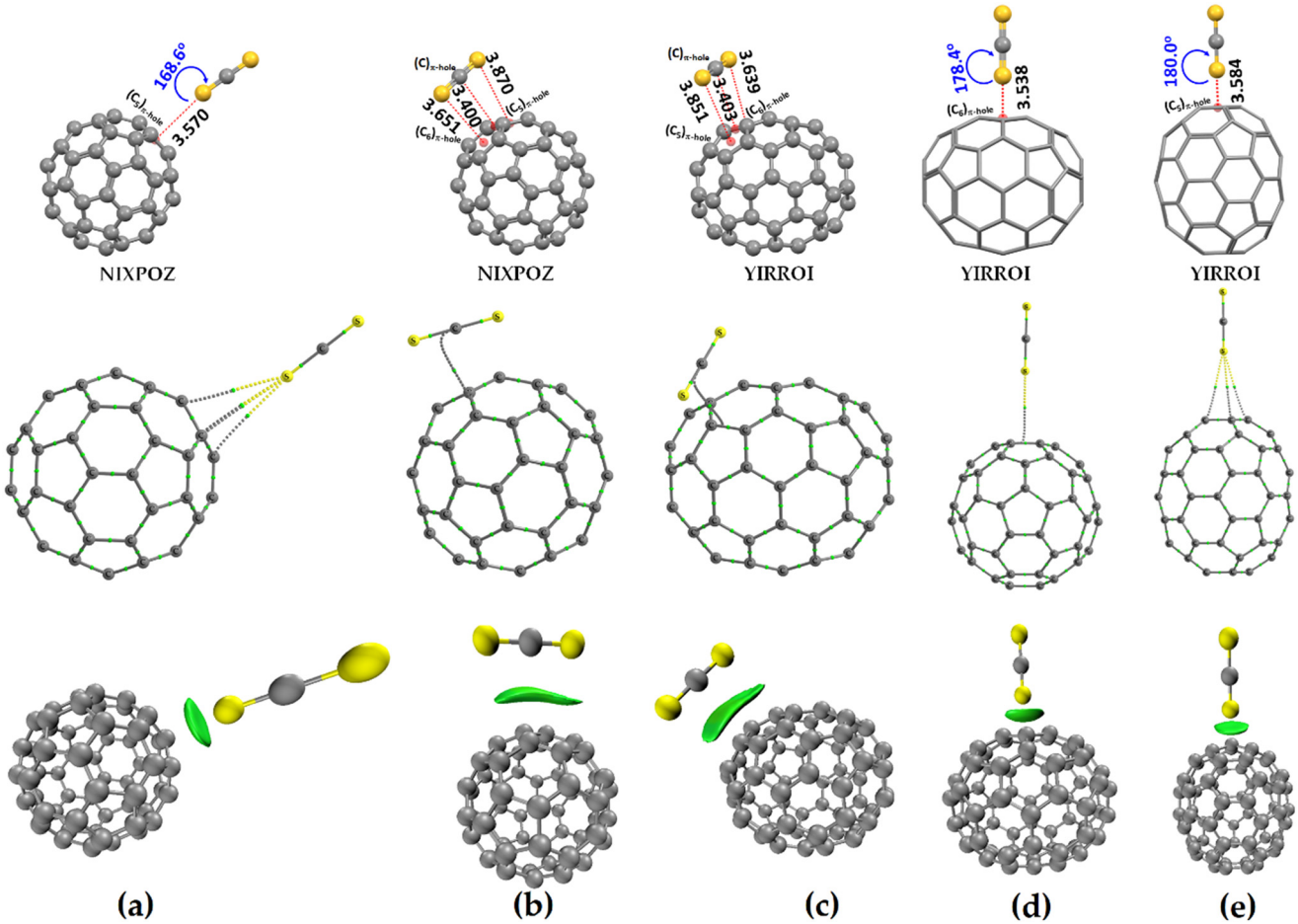


Fig. 20 (Top) Ball-and-stick models of the [ωB97XD/cc-pVTZ] level fully-relaxed geometries of C_{60} and C_{70} with CS_2: (a) and (b) [C_{60}, (CS_2)]; (c)–(e) [C_{70}, (CS_2)]; selected bond lengths and bond angles are in Å and degrees, respectively. (Middle) The QTAIM-based molecular graphs of the corresponding systems, respectively, with bond paths in atom color and bond critical points as tiny spheres in green. (Bottom) Illustration of the IGM-δg^{inter} isosurfaces (green volumes) corresponding systems, respectively, with isovalues of 0.010 a.u. The CSD reference is shown in uppercase letters, and centroids are tiny red spheres.

= 175.8°) is present in the crystal between C_{70} and I_2, yet in the DFT geometry the I···(C═C)$_\pi$ halogen bond occurs between the axial σ-hole on I along the I–I covalent bond extension and negative π density delocalized on the C═C bond common to a pair of C_6 and C_5 rings (r(I···(C═C)$_{\pi\text{-hole}}$) = 3.326 Å and ∠I–I···(C═C)$_{\pi\text{-hole}}$ = 187.7°). A very similar result was found for the other geometry of the same system shown in Fig. 21b, but in this case the dominant interaction is also a $(C_6)_{\pi\text{-hole}}$···I halogen bond that occurs between the centroid electrophilic (π-hole) portion of a C_6 ring and the lateral negative portion of I in I_2. The remaining interaction between the interacting units of this latter system is secondary, which is a forced consequence of the former (primary) interaction.

In the case of the anion-molecule system shown in Fig. 21c, the gas-phase geometry is more distorted compared to that found in the crystalline phase. We relaxed two geometries of the same system, one with the anion lying perpendicular to the surface of the C═C of a C_5 ring and the other close to a geometry shown in Fig. 21c, as observed in the crystalline phase. Both the initial geometries of the [C_{70}, I_3^-] system resulted to the structure shown in Fig. 21c. The mismatch between the gas-phase and solid-state geometries is not very surprising since packing forces absent in the gas-phase probably play an important role in rearranging the two molecules in the solid state. Nevertheless, our calculation suggests that the formation of the binary complex driven by the $(C_6)_{\pi\text{-hole}}$···I type π-hole centered interaction in Fig. 21b is more stable than that was driven by the σ-hole interaction shown in Fig. 21a (ΔE values −4.76 kcal mol^{-1} *vs.* −4.26 kcal mol^{-1}). Clearly, either of these interaction energies is smaller than that of the anion-molecule system, with ΔE = −11.15 kcal mol^{-1}. All the intermolecular interactions rationalized based on intermolecular geometries are consistent with the IGM-δg^{inter} isosurface plots shown in Fig. 21a and b (bottom).

The BSSE corrected interaction energy for the binary complex between the $C_{50}H_{10}$ carbon nanotube and CS_2 was −1.93 and −13.35 kcal mol^{-1} for the two conformations shown in Fig. 22a and b, respectively. This difference in the interaction energy is not unexpected given that the

 This journal is © The Royal Society of Chemistry 2023

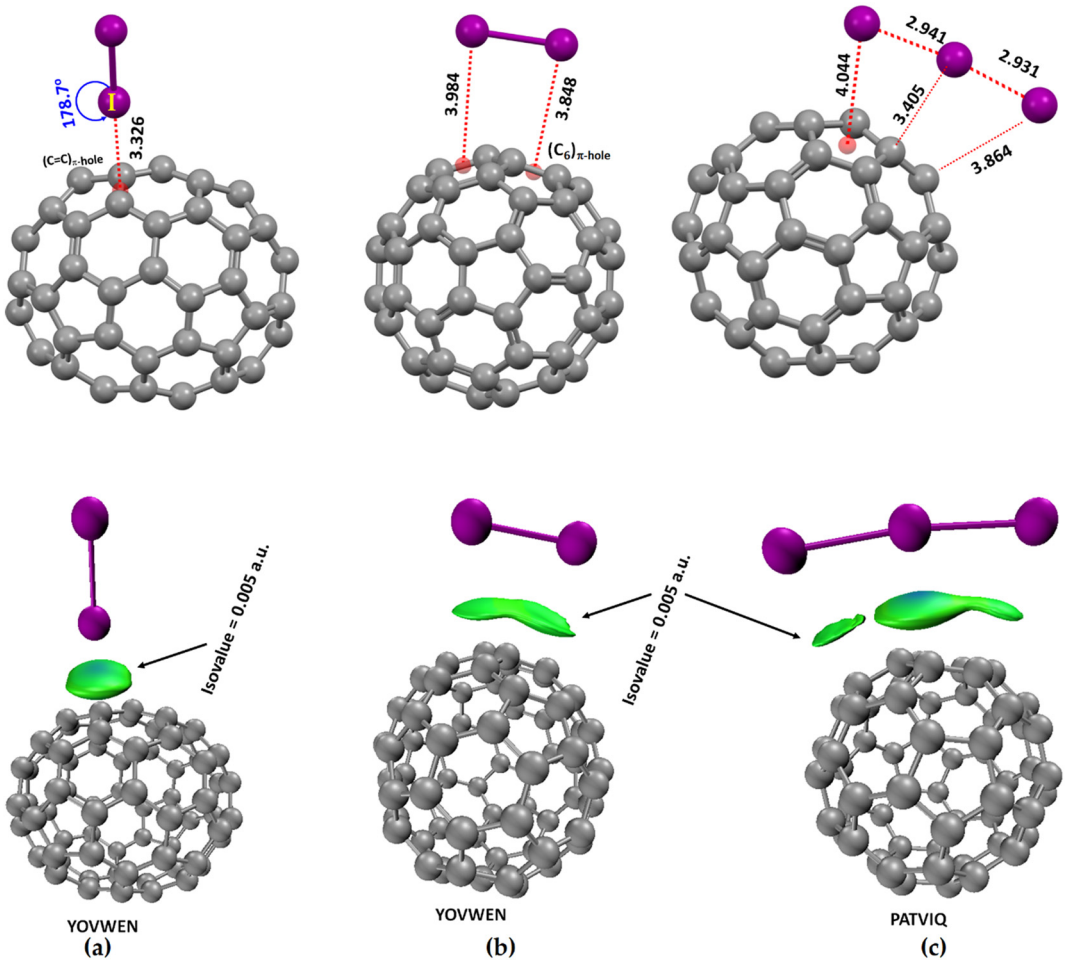


Fig. 21 The [ωB97XD/cc-pVTZ] level optimized geometry (top), and IGM-δg^{inter} based isosurfaces (bottom) of (a) and (b) $C_{70}\cdots I_2$, and (c) $C_{70}\cdots I_3^-$. Selected bond distances are in Å and, the IGM-δg^{inter} isosurfaces (green volumes, bottom) correspond to the 0.005 a.u. isosurface. Bluish and green IGM-δg^{inter} isosurfaces signifies the presence of medium strength and weak interactions, respectively. The CSD reference code is marked for each case in uppercase letters, and the intermolecular interactions are shown as dotted lines in red.

interaction is more localized when a single S atom in CS_2 is in attractive engagement with the outer surface of a C_6 ring. When the molecule is inside the open cage, all parts of the molecule are in attractive engagement with the interior carbon framework of the nanotube, which is evident not only from the many-fold bond paths between CS_2 and C═C bonds obtained from a QTAIM analysis (Fig. 22a, top, right), but also a close-ended tube-like isosurface between the two interacting molecules (Fig. 22b, bottom).

One of the limitations of QTAIM is that it does not show any bond path between the center of an arene moiety, where a (3+, 1) rcp is found, and the nucleophile that attract each other, leading to the formation of an intermolecular interaction. Rather, it shows bond paths between the electron density donor atom and the carbon framework of the arene moiety only. The QTAIM results are also consistent with an NBO second order analysis that provides insight into the nature of charge transfer interactions between electron density acceptors associated with the π* orbitals of the fullerene system and the electron density donors associated with the lone-pair orbitals of the interacting molecule (*viz.* CS_2), yet in disagreement with the conclusions of the MESP model which suggests direct interaction between the centroids of the positive potentials with the interacting nucleophile.

Our calculation suggests that the $(C_5)_\pi\cdots CO$ interaction, Fig. 18b, is a result of charge transfer delocalization from the π-type bonding orbital of (C≡O) to the BD*(2) (C═C) delocalized anti-bonds of the C_5 ring in $(C_{20})_\pi\cdots CO$, as well as that to the Rydberg (RY) type orbital RY*(C). The $E^{(2)}$ for the corresponding charge transfer delocalizations were 0.1 and 0.37/0.75 kcal mol^{-1}, respectively. A very similar result was obtained for $(C_{20})_\pi\cdots N_2$, Fig. 18a, but in this case $E^{(2)}$ for the delocalizations BD (N≡N) → BD* (C═C) and BD (3) (N≡N) → RY* (C) were roughly around 0.1 kcal mol^{-1}. However, in the case of $(C_{20})_\pi\cdots Cl_2/(C_{20})_\pi\cdots Br_2$, Fig. 18c/d, for examples, the $E^{(2)}$ associated with LP(3) (Cl)/LP(3) (Br) → BD* (C═C) were appreciably larger than that calculated for LP(2) (Cl)/LP(3) (Br)

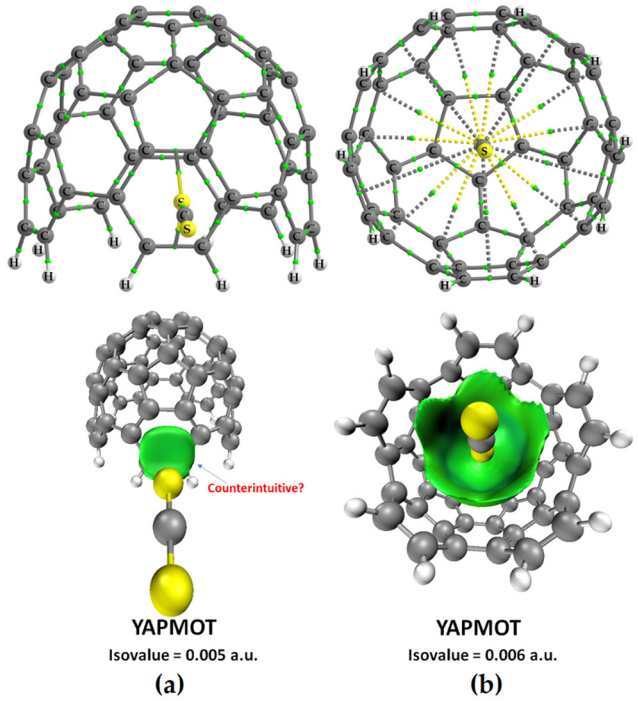


Fig. 22 The [ωB97XD/cc-pVTZ] level QTAIM molecular graphs (top) and IGM-δg^{inter} isosurfaces (bottom) for the $C_{50}H_{10}$ carbon nanotube and CS_2 binary complex system. The orientation of the CS_2 molecule in (a) and (b) is similar to those observed in the crystal. The bond paths and bond critical points leading to the molecular graphs are shown as solid and dotted lines in atom color. Green IGM-δg^{inter} isosurfaces signifies the presence of weak interactions.

→ RY* (C) (values 0.1 *vs.* 1.0/0.8 kcal mol^{-1}), where LP and BD refer to the lone-pair and bonding orbitals, respectively.

The NBO second order analysis suggested that the charge transfer delocalization for the H-bonded dimers shown in Fig. 17a–c can be described primarily as BD(π) (C═C) → σ*(HX), and the largest of energies $E^{(2)}$ associated with them were 5.08, 3.65, and 3.55, kcal mol^{-1} for FH···$(C_{20})_\pi$, ClH···$(C_{20})_\pi$, and BrH···$(C_{20})_\pi$, respectively. These are in line with the trend in the interaction energies of the corresponding binary systems shown in Fig. 17a–c, respectively (*cf.* Table 2 for ΔE or ΔE (BSSE) values). The $E^{(2)}$ for charge transfer delocalizations LP(1) C → LP*(1) H(F), [BD(σ)(C═C) → BD*(H–Cl); BD(π)(C═C) → BD*(H–Cl)], and [LP(1)(Br) → BD*(C–H); LP(4)(Br) → BD*(C–H)], were 72.59, [4.0; 23.24], and [7.63; 68.65] kcal mol^{-1} for dimers shown in Fig. 17d–f, respectively. These are also consistent with the trend in the interaction energies of the corresponding dimeric complexes summarized in Table 2.

The results shown above provide evidence of intermolecular interactions between the interacting units, yet they are not fully in agreement with the results of the MESP model which describes the intermolecular interaction in terms of the positive centroid region of the C_5 ring in C_{20} and negative lone-pair regions in the diatomic molecules that are interacting with each other. This can be appreciated from the results presented in Fig. 19, which show that the electrophilic π-hole on the C_5 ring of C_{20} molecule is in attractive engagement with the lateral negative sites of F_2, N_2, and CO, resulting in the formation of binary complexes. Whereas these interactions are evident in terms of $(C{=}C)_\pi\cdots F(F_2)$, $(C{=}C)_\pi\cdots N(N_2)$ and $(C{=}C)_\pi\cdots C/O(CO)$ bond paths emerged from a QTAIM analysis, they might be regarded as localized interactions. From an IGM-δg^{inter} analysis, however, one should deduce that these interactions are delocalized by nature and will appear as flat isosurfaces between the C_5 ring of the C_{20} fullerene and the interacting basins of the nucleophilic sites. Interestingly, the MESP model-based conclusions are in reasonable agreement with the nature of the IGM-δg^{inter} isosurface volumes developed between the interacting electron density donor and acceptor moieties (Fig. 18a–e, bottom) that are flat, irregular and circular, providing evidence that the non-covalent interactions are not localized as suggested by NBO and QTAIM.

Conclusion

In this study, the MESP model was used to determine the nature of the electrostatic surfaces of various models of fullerene, carbon nanotube, and graphene. This was used to provide an explanation of the self-organization of a variety of carbon-based molecules, leading to the development of various functional materials. With the exception of hydrogen-terminated graphene, nanotubes of chirality (4, 0), the SWCNT of chirality (4, 4) and length 3.0 (periodic units), and the buckycatcher, no carbonaceous systems were found that comprise pentagonal or hexagonal rings with negative electrostatic potentials at the centroid regions. We have shown that the C–C atom–atom pairs in the C_5 and C_6 rings of fullerenes and carbon nanotubes that exhibited a high value of delocalization index are associated with negative electrostatic potentials (negative π-holes) on their electrostatic surfaces, a unique finding that, to our knowledge, has not been explored. In the majority of the systems investigated, it was found that the electrostatic surfaces of the C_5 and C_6 rings consist of weak-to-moderate strength electrophilic π-holes and C═C bonding region conceive nucleophilic π-holes. These are a vital aspect of the surfaces of carbonaceous molecules that play an important role as π-centered tetrel bond donors and acceptors of interacting electrophiles (hydrogen- and halogen bonds, *etc.*) in self-assembly, thereby shaping a variety of crystalline materials *via* coulombic attraction. The illustrative crystal systems analyzed in this study are intended to guide researchers in different research fields to identify electrophilic and nucleophilic π-holes in carbonaceous systems. It should be emphasized that the MESP plot representing any given system has different maxima and minima of potential than that shown for the other system, yet they are represented by the same red and blue colors, respectively. Although the application of NBO and QTAIM approaches to the model delocalized systems has been shown to be effective in rationalizing the origin of intermolecular interactions in them, the MESP model-based

 This journal is © The Royal Society of Chemistry 2023

conclusions of the intermolecular interactions in some illustrative binary complex systems were shown to be effective and are in accord with representative isosurfaces that emerged from an IGM-δg^{inter} analysis.

Institutional Review Board statement

Not applicable.

Informed consent statement

Not applicable.

Data availability statement

This research did not report any data.

Author contributions

Conceptualization, project design, and project administration, P. R. V.; formal analysis and investigation, P. R. V. and A. V.; supervision, P. R. V.; writing—original draft, P. R. V. and A. V.; validation, visualization and writing—review and editing, P. R. V., H. M., A. V., and K. Y. All authors have read and agreed to the published version of the manuscript.

Conflicts of interest

The authors declare no conflict of interest. The funders had absolutely no role in the design of the study; in the collection, analyses, or interpretation of data; in the writing of the manuscript; or in the decision to publish the results.

Acknowledgements

This research received no external funding. This work was entirely conducted using the various computation and laboratory facilities provided by the University of Tokyo and the University of the Witwatersrand. P. R. V. is currently affiliated with the University of the Witwatersrand (SA) and Nagoya University (Japan). A. V. is currently affiliated with Tokyo University of Science (Japan). K. Y. is currently affiliated with Yokohama City University (Japan).

References

1 H. W. Kroto, J. R. Heath, S. C. O'Brien, R. F. Curl and R. E. Smalley, *Nature*, 1985, **318**, 162–163.
2 L. Hou, X. Cui, B. Guan, S. Wang, R. Li, Y. Liu, D. Zhu and J. Zheng, *Nature*, 2022, **606**, 507–510.
3 S. Iijima and T. Ichihashi, *Nature*, 1993, **363**, 603–605.
4 S. Iijima, *Nature*, 1991, **354**, 56–58.
5 K. S. Novoselov, A. K. Geim, S. V. Morozov, D. Jiang, Y. Zhang, S. V. Dubonos, I. V. Grigorieva and A. A. Firsov, *Science*, 2004, **306**, 666–669.
6 Y. Zhu, S. Gao and N. Hosmane, in *Comprehensive Energy Systems*, ed. I. Dincer, Elsevier, Oxford, 2018, pp. 40–71.
7 N. López-Salas and M. Antonietti, *Bull. Chem. Soc. Jpn.*, 2021, **94**, 2822–2828.
8 H. Terrones and M. Terrones, *New J. Phys.*, 2003, **5**, 126.
9 X. Ye, C. Lendel, M. Langton, R. T. Olsson and M. S. Hedenqvist, in *Industrial Applications of Nanomaterials*, ed. S. Thomas, Y. Grohens and Y. B. Pottathara, Elsevier, 2019, pp. 29–63.
10 S. Z. Al Sheheri, Z. M. Al-Amshany, Q. A. Al Sulami, N. Y. Tashkandi, M. A. Hussein and R. M. El-Shishtawy, *Des. Monomers Polym.*, 2019, **22**, 8–53.
11 A. D. D. Oliveira and C. A. G. Beatrice, *Polymer Nanocomposites with Different Types of Nanofiller*, IntechOpen, 2018.
12 T. Kuzumaki, in *Polymer Nanocomposites*, ed. Y.-W. Mai and Z.-Z. Yu, Woodhead Publishing, 2006, pp. 359–388.
13 J. Chen, B. Liu, X. Gao and D. Xu, *RSC Adv.*, 2018, **8**, 28048–28085.
14 J. Nelson, *Mater. Today*, 2011, **14**, 462–470.
15 R. Ganesamoorthy, G. Sathiyan and P. Sakthivel, *Sol. Energy Mater. Sol. Cells*, 2017, **161**, 102–148.
16 S. Collavini and J. L. Delgado, *Sustainable Energy Fuels*, 2018, **2**, 2480–2493.
17 Q.-H. Zhang, W.-D. Hu, X.-F. Wang, G. Chen, J.-P. Zhang, L.-X. Xiao and T. Miyasaka, *Chem. Lett.*, 2017, **46**, 101–103.
18 Y. Zhang, I. Murtaza and H. Meng, *J. Mater. Chem. C*, 2018, **6**, 3514–3537.
19 S. Yao, X. Yuan, L. Jiang, T. Xiong and J. Zhang, *Materials*, 2020, **13**, 2924.
20 R. Partha and J. L. Conyers, *Int. J. Nanomed.*, 2009, **4**, 261–275.
21 I. Rašović, *Mater. Sci. Technol.*, 2017, **33**, 777–794.
22 R. Bakry, R. M. Vallant, M. Najam-ul-Haq, M. Rainer, Z. Szabo, C. W. Huck and G. K. Bonn, *Int. J. Nanomed.*, 2007, **2**, 639–649.
23 P. Rozhin, C. Charitidis and S. Marchesan, *Molecules*, 2021, **26**, 4084.
24 N. V. Kamanina and N. V. Kamanina, *Introductory Chapter: Why the Study of Fullerenes is so Important?*, IntechOpen, 2018.
25 D.-M. Tang, S. V. Erohin, D. G. Kvashnin, V. A. Demin, O. Cretu, S. Jiang, L. Zhang, P.-X. Hou, G. Chen, D. N. Futaba, Y. Zheng, R. Xiang, X. Zhou, F.-C. Hsia, N. Kawamoto, M. Mitome, Y. Nemoto, F. Uesugi, M. Takeguchi, S. Maruyama, H.-M. Cheng, Y. Bando, C. Liu, P. B. Sorokin and D. Golberg, *Science*, 2021, **374**, 1616–1620.
26 J. Tomada, T. Dienel, F. Hampel, R. Fasel and K. Amsharov, *Nat. Commun.*, 2019, **10**, 3278.
27 F. Yang, M. Wang, D. Zhang, J. Yang, M. Zheng and Y. Li, *Chem. Rev.*, 2020, **120**, 2693–2758.
28 R.-I. Stefan-van Staden and I. R. Comnea-Stancu, *Chirality*, 2021, **33**, 51–58.
29 B. Liu, F. Wu, H. Gui, M. Zheng and C. Zhou, *ACS Nano*, 2017, **11**, 31–53.

30 M. N. Norizan, M. H. Moklis, S. Z. N. Demon, N. A. Halim, A. Samsuri, I. S. Mohamad, V. F. Knight and N. Abdullah, *RSC Adv.*, 2020, **10**, 43704–43732.
31 R. Alshehri, A. M. Ilyas, A. Hasan, A. Arnaout, F. Ahmed and A. Memic, *J. Med. Chem.*, 2016, **59**, 8149–8167.
32 S. Merum, J. B. Veluru and R. Seeram, *Mater. Sci. Eng., B*, 2017, **223**, 43–63.
33 J. Cayssol, *C. R. Phys.*, 2013, **14**, 760–778.
34 E. F. Sheka, *Rev. Adv. Mater. Sci.*, 2018, **53**, 1–28.
35 K. K. Jena, A. T. Mayyas, B. Mohanty, B. K. Jena, J. R. Jos, A. AlFantazi, B. Chakraborty and A. A. Almarzooqi, *Energy Fuels*, 2022, **36**, 2159–2170.
36 J. Ajuria, M. Zarrabeitia, M. Arnaiz, O. Urra, T. Rojo and E. Goikolea, *J. Electrochem. Soc.*, 2019, **166**, A2840.
37 H. Kim, K.-Y. Park, J. Hong and K. Kang, *Sci. Rep.*, 2014, **4**, 5278.
38 X. Zhou, X. Chen, H. Zhu, X. Dong, L. Li, G. Cheng, Z. Zhang, X. Hu, N. Yuan and J. Ding, *Nanoscale*, 2021, **13**, 8304–8312.
39 M. Ye, Z. Zhang, Y. Zhao and L. Qu, *Joule*, 2018, **2**, 245–268.
40 H. Huang, S. Su, N. Wu, H. Wan, S. Wan, H. Bi and L. Sun, *Front. Chem.*, 2019, **7**, 399.
41 S. Z. N. Demon, A. I. Kamisan, N. Abdullah, S. A. M. Noor, O. K. Khim, N. A. M. Kasim, M. Z. A. Yahya, N. A. A. Manaf, A. F. M. Azmi and N. A. Halim, *Sens. Mater.*, 2020, **32**, 759.
42 Q. Burlingame, C. Coburn, X. Che, A. Panda, Y. Qu and S. R. Forrest, *Nature*, 2018, **554**, 77–80.
43 *Cambridge Structural Database (CSD)*, Cambridge, UK, 2022.
44 C. R. Groom, I. J. Bruno, M. P. Lightfoot and S. C. Ward, *Acta Crystallogr., Sect. B: Struct. Sci., Cryst. Eng. Mater.*, 2016, **72**, 171–179.
45 P. R. Varadwaj, A. Varadwaj, H. M. Marques and K. Yamashita, *CrystEngComm*, 2023, **25**, 1411–1423.
46 D. Shin and Y. Jung, *Phys. Chem. Chem. Phys.*, 2022, **24**, 25740–25752.
47 C. H. Suresh, G. S. Remya and P. K. Anjalikrishna, *WIREs Comput. Mol. Sci.*, 2022, **12**, e1601.
48 R. Vetrivel, R. C. Deka, A. Chatterjee, M. Kubo, E. Broclawik and A. Miyamoto, in *Theoretical and Computational Chemistry*, ed. J. S. Murray and K. Sen, Elsevier, 1996, vol. 3, pp. 509–541.
49 J. S. Murray and P. Politzer, in *Molecular Orbital Calculations for Biological Systems*, ed. A.-M. Sapse, Oxford University Press, 1998, pp. 49–84.
50 L. Liu, L. Miao, L. Li, F. Li, Y. Lu, Z. Shang and J. Chen, *J. Phys. Chem. Lett.*, 2018, **9**, 3573–3579.
51 P. Politzer, P. R. Laurence and K. Jayasuriya, *Environ. Health Perspect.*, 1985, **61**, 191–202.
52 R. F. W. Bader, *Atoms in Molecules*, **https://www.wiley.com/legacy/wileychi/ecc/samples/sample02.pdf**, (accessed May 21, 2023).
53 R. F. W. Bader, *Acc. Chem. Res.*, 1985, **18**, 9–15.
54 R. F. W. Bader, in *Encyclopedia of Computational Chemistry*, ed. P. V. Schleyer, John Wiley and Sons, Chichester, UK, 1998, vol. 1, pp. 64–86.
55 P. Politzer and J. S. Murray, *J. Comput. Chem.*, 2018, **39**, 464–471.
56 P. Politzer and J. S. Murray, *Crystals*, 2017, **7**(7), 212.
57 P. R. Varadwaj, A. Varadwaj and B.-Y. Jin, *Phys. Chem. Chem. Phys.*, 2015, **17**, 31624–31645.
58 A. Varadwaj, H. M. Marques and P. R. Varadwaj, *Molecules*, 2019, **24**, 379.
59 A. Varadwaj, H. M. Marques and P. R. Varadwaj, *J. Comput. Chem.*, 2019, **40**, 1836–1860.
60 A. Varadwaj, P. R. Varadwaj, H. M. Marques and K. Yamashita, *Molecules*, 2022, **27**, 3421.
61 P. R. Varadwaj, A. Varadwaj, H. M. Marques and K. Yamashita, *Molecules*, 2022, **27**, 1487.
62 P. R. Varadwaj, A. Varadwaj, H. M. Marques and K. Yamashita, *Compounds*, 2022, **2**, 80–110.
63 P. R. Varadwaj, A. Varadwaj and H. M. Marques, *Inorganics*, 2019, **7**, 40.
64 F. Weinhold, *J. Comput. Chem.*, 2012, **33**, 2363–2379.
65 C. Lefebvre, G. Rubez, H. Khartabil, J.-C. Boisson, J. Contreras-García and E. Hénon, *Phys. Chem. Chem. Phys.*, 2017, **19**, 17928–17936.
66 C. Lefebvre, H. Khartabil, J.-C. Boisson, J. Contreras-García, J.-P. Piquemal and E. Hénon, *ChemPhysChem*, 2018, **19**, 724–735.
67 Z. Wang, X. Ke, Z. Zhu, F. Zhu, M. Ruan, H. Chen, R. Huang and L. Zheng, *Phys. Lett. A*, 2001, **280**, 351–356.
68 W. An, Y. Gao, S. Bulusu and X. C. Zeng, *J. Chem. Phys.*, 2005, **122**, 204109.
69 A. Devos and M. Lannoo, *Phys. Rev. B: Condens. Matter Mater. Phys.*, 1998, **58**, 8236–8239.
70 F. N. Ajeel, M. H. Mohammed and A. M. Khudhair, *Russ. J. Phys. Chem. B*, 2017, **11**, 850–858.
71 K. E. Riley, K.-A. Tran, P. Lane, J. S. Murray and P. Politzer, *J. Compos. Sci.*, 2016, **17**, 273–284.
72 Y. F. Chang, J. P. Zhang, H. Sun, B. Hong, Z. An and R. S. Wang, *Int. J. Quantum Chem.*, 2005, **105**, 142–147.
73 A. I. Melker and A. N. Matvienko, *Mater. Phys. Mech.*, 2020, **45**, 49–59.
74 D. A. García-Hernández, S. Iglesias-Groth, J. A. Acosta-Pulido, A. Manchado, P. García-Lario, L. Stanghellini, E. Villaver, R. A. Shaw and F. Cataldo, *Astrophys. J.*, 2011, **737**, L30.
75 A. V. Silant'ev, *Phys. Met. Metallogr.*, 2020, **121**, 195–201.
76 B. T. Tomić, C. S. Abraham, S. Pelemiš, S. J. Armaković and S. Armaković, *Phys. Chem. Chem. Phys.*, 2019, **21**, 23329–23337.
77 D. Tomanek and N. Frederick, **https://nanotube.msu.edu/fullerene/fullerene.php?C=44**.
78 M. Lyons, B. I. Dunlap, D. W. Brenner, D. H. Robertson, R. C. Mowrey, J. W. Mintmire and C. T. White, in *Physics and Chemistry of Finite Systems: From Clusters to Crystals*, ed. P. Jena, S. N. Khanna and B. K. Rao, Springer Netherlands, Dordrecht, 1992, pp. 1347–1351.
79 C. T. White, M. Lyons, D. W. Brenner, J. W. Mintmire, D. H. Robertson, R. C. Mowrey and B. I. Dunlap, *MRS Online Proc. Libr.*, 1994, **349**, 331–336.
80 J. C. Dobrowolski, *ACS Omega*, 2019, **4**, 18699–18710.

 This journal is © The Royal Society of Chemistry 2023

81 J. Kruszewski and T. M. Krygowski, *Tetrahedron Lett.*, 1972, **13**, 3839–3842.
82 T. M. Krygowski, H. Szatylowicz, O. A. Stasyuk, J. Dominikowska and M. Palusiak, *Chem. Rev.*, 2014, **114**, 6383–6422.
83 E. Matito, M. Duran and M. Solà, *J. Chem. Phys.*, 2005, **122**, 014109.
84 H. Szatylowicz, P. A. Wieczorkiewicz and T. M. Krygowski, *Science*, 2022, **4**, 24.
85 A. R. Khamatgalimov, L. I. Yakupova and V. I. Kovalenko, *Theor. Chem. Acc.*, 2020, **139**, 159.
86 J. Guan, Z. Jin, Z. Zhu, C. Chuang, B.-Y. Jin and D. Tománek, *Phys. Rev. B: Condens. Matter Mater. Phys.*, 2014, **90**, 245403.
87 D. Tomanek, **https://nanotube.msu.edu/fullerene/fullerene-isomers.html**.
88 J. López-Andarias, A. Frontera and S. Matile, *J. Am. Chem. Soc.*, 2017, **139**, 13296–13299.
89 E. C. Escudero-Adán, A. Bauzá, L. P. Hernández-Eguía, F. Würthner, P. Ballester and A. Frontera, *CrystEngComm*, 2017, **19**, 4911–4919.
90 M. D. Esrafili, A. A. Khan and P. Mousavian, *RSC Adv.*, 2021, **11**, 22598–22610.
91 F. Gao, G.-L. Zhao, S. Yang and J. J. Spivey, *J. Am. Chem. Soc.*, 2013, **135**, 3315–3318.
92 S. H. Noh, C. Kwon, J. Hwang, T. Ohsaka, B.-J. Kim, T.-Y. Kim, Y.-G. Yoon, Z. Chen, M. H. Seo and B. Han, *Nanoscale*, 2017, **9**, 7373–7379.
93 D. L. Dorset and M. P. McCourt, *Acta Crystallogr., Sect. A: Found. Crystallogr.*, 1994, **50**, 344–351.
94 AMCSD Search Results for Buckminsterfullerene, **https://rruff.geo.arizona.edu/AMS/minerals/Buckminsterfullerene**, (accessed 3 November 2022).
95 S. Alvarez, *Dalton Trans.*, 2013, **42**, 8617–8636.
96 M. Fujiwara, T. Kambe and K. Oshima, *Phys. Rev. B: Condens. Matter Mater. Phys.*, 2005, **71**, 174424.
97 B. B. Iversen, A. Darovsky, R. Bolotovsky and P. Coppens, *Acta Crystallogr., Sect. B: Struct. Sci.*, 1998, **54**, 174–179.
98 N. G. Spitsina, S. V. Konovalikhin, A. S. Lobach, G. V. Shilov and O. A. D'Yachenko, *Russ. Chem. Bull.*, 1999, **48**, 2273–2278.
99 D. Pham, J. Cerón Bertran, M. M. Olmstead, M. Mascal and A. L. Balch, *Org. Lett.*, 2005, **7**, 2805–2808.
100 G. A. Domrachev, Y. A. Shevelev, V. K. Cherkasov, G. K. Fukin, G. V. Markin and A. I. Kirillov, *Russ. Chem. Bull.*, 2006, **55**, 225–229.
101 M. Yanney, F. R. Fronczek and A. Sygula, *Angew. Chem., Int. Ed.*, 2015, **54**, 11153–11156.
102 S.-Z. Zhan, J.-H. Li, G.-H. Zhang, M.-D. Li, S. Sun, J. Zheng, G.-H. Ning, M. Li, D.-B. Kuang, X.-D. Wang and D. Li, *Chem. Commun.*, 2020, **56**, 3325–3328.
103 A. Sygula, F. R. Fronczek, R. Sygula, P. W. Rabideau and M. M. Olmstead, *J. Am. Chem. Soc.*, 2007, **129**, 3842–3843.
104 P. R. Varadwaj, A. Varadwaj and H. M. Marques, *Sci. Rep.*, 2019, **9**, 10650.
105 H. Takahashi, E. Matsubara, M. Shiro, S. Matsubara, N. Sato, A. Muramatsu and K. Tohji, *Fullerenes, Nanotubes, Carbon Nanostruct.*, 2002, **10**, 217–226.
106 Z. Sun, T. Mio, T. Okada, T. Matsuno, S. Sato, H. Kono and H. Isobe, *Angew. Chem., Int. Ed.*, 2019, **58**, 2040–2044.
107 F. L. Bowles, B. Q. Mercado, K. B. Ghiassi, S. Y. Chen, M. M. Olmstead, H. Yang, Z. Liu and A. L. Balch, *Cryst. Growth Des.*, 2013, **13**, 4591–4598.
108 P. Ares and K. S. Novoselov, *Nano Mater. Sci.*, 2022, **4**, 3–9.
109 Z.-F. Liang, S.-L. Ma, H.-T. Xue, F. Ding, J. L. Liu and F.-L. Tang, *Chin. Phys. B*, 2018, **27**, 016801.
110 A. D. Zdetsis and E. N. Economou, *J. Phys. Chem. C*, 2015, **119**, 16991–17003.
111 I. A. Popov, K. V. Bozhenko and A. I. Boldyrev, *Nano Res.*, 2012, **5**, 117–123.
112 Y. B. Apriliyanto, S. Battaglia, S. Evangelisti, N. Faginas-Lago, T. Leininger and A. Lombardi, *J. Phys. Chem. A*, 2021, **125**, 9819–9825.
113 D. Malko, C. Neiss, F. Viñes and A. Görling, *Phys. Rev. Lett.*, 2012, **108**, 086804.
114 Q. Peng, A. K. Dearden, J. Crean, L. Han, S. Liu, X. Wen and S. De, *Nanotechnol., Sci. Appl.*, 2014, **7**, 1–29.
115 B. G. Kim and H. J. Choi, *Phys. Rev. B: Condens. Matter Mater. Phys.*, 2012, **86**, 115435.
116 Y. Li, L. Xu, H. Liu and Y. Li, *Chem. Soc. Rev.*, 2014, **43**, 2572–2586.
117 L. Guo, J. D. Bradshaw, C. A. Tessier and W. J. Youngs, *J. Chem. Soc., Chem. Commun.*, 1994, 243–244, DOI: **10.1039/C39940000243**.
118 X. Qiu, D. Xu, T. Lin, X. Yang, Y. Liu and P. He, *Mater. Trans.*, 2015, **56**, 1007–1009.
119 M. S. Arefin, *Nanomaterials*, 2013, **3**, 1–21.
120 R. F. Rajter, R. H. French, W. Y. Ching, R. Podgornik and V. A. Parsegian, *RSC Adv.*, 2012, **3**, 823–842.
121 D. J. Doren and J. T. Frey, *TubeGen Online - v3.4*, University of Delaware, Newark DE, 2011, **https://turin.nss.udel.edu/research/tubegenonline.html**, (accessed 1 November 2022).
122 *Avogadro: an open-source molecular builder and visualization tool, Version 1.XX*, **https://avogadro.cc/cite/**, (accessed 10 November 2022).
123 B. M. Wong and J. W. Lee, *J. Phys. Chem. Lett.*, 2011, **2**, 2702–2706.
124 H.-B. Li, A. J. Page, S. Irle and K. Morokuma, *J. Am. Chem. Soc.*, 2012, **134**, 15887–15896.
125 K. M. Liew, J.-W. Yan and L.-W. Zhang, in *Mechanical Behaviors of Carbon Nanotubes*, ed. K. M. Liew, J.-W. Yan and L.-W. Zhang, Elsevier, 2017, pp. 411–442.
126 C. D. Zeinalipour-Yazdi and E. Z. Loizidou, *Carbon*, 2017, **115**, 819–827.
127 C. B. Larsen and N. T. Lucas, *Chem. N. Z.*, 2012, **75**, 49–55.
128 L. T. Scott, E. A. Jackson, Q. Zhang, B. D. Steinberg, M. Bancu and B. Li, *J. Am. Chem. Soc.*, 2012, **134**, 107–110.
129 K. Ikemoto, R. Kobayashi, S. Sato and H. Isobe, *Org. Lett.*, 2017, **19**, 2362–2365.
130 S. Sato, T. Yamasaki and H. Isobe, *Proc. Natl. Acad. Sci. U. S. A.*, 2014, **111**, 8374–8379.

131 F.-G. Klärner and T. Schrader, *Acc. Chem. Res.*, 2013, **46**, 967–978.
132 T. Matsuno, S. Sato, R. Iizuka and H. Isobe, *Chem. Sci.*, 2015, **6**, 909–916.
133 P. R. Varadwaj, A. Varadwaj and H. M. Marques, *Sci. Rep.*, 2019, **9**, 10650.
134 H. Kawabata and H. Tachikawa, *C*, 2017, **3**, 15.
135 G. Praveena and P. Kolandaivel, *J. Mol. Struct.*, 2007, **828**, 154–161.
136 T. T. Vehviläinen, M. G. Ganchenkova, L. E. Oikkonen and R. M. Nieminen, *Phys. Rev. B*, 2011, **84**, 085447.
137 J. S. Murray, Z. P.-I. Shields, P. G. Seybold and P. Politzer, *J. Comput. Sci.*, 2015, **10**, 209–216.
138 C. Wang, D. Danovich, S. Shaik, W. Wu and Y. Mo, *J. Comput. Chem.*, 2019, **40**, 1015–1022.
139 P. R. Varadwaj, A. Varadwaj, H. M. Marques and K. Yamashita, *Computation*, 2018, **6**, 51.
140 S. V. Konovalikhin, O. A. D'yachenko, G. V. Shilov, N. G. Spitsina, K. V. Van and E. B. Yagubskii, *Izv. Akad. Nauk SSSR, Ser. Khim.*, 1997, **46**, 1480–1483.
141 K. B. Ghiassi, F. L. Bowles, S. Y. Chen, M. M. Olmstead and A. L. Balch, *Cryst. Growth Des.*, 2014, **14**, 5131–5136.
142 D. V. Konarev, S. S. Khasanov, A. Otsuka, G. Saito and R. N. Lyubovskaya, *Synth. Met.*, 2005, **151**, 231–238.

 This journal is © The Royal Society of Chemistry 2023